iScience

CellPress
OPEN ACCESS

Article

Integrating Systems Biology and an *Ex Vivo* Human Tumor Model Elucidates PD-1 Blockade Response Dynamics

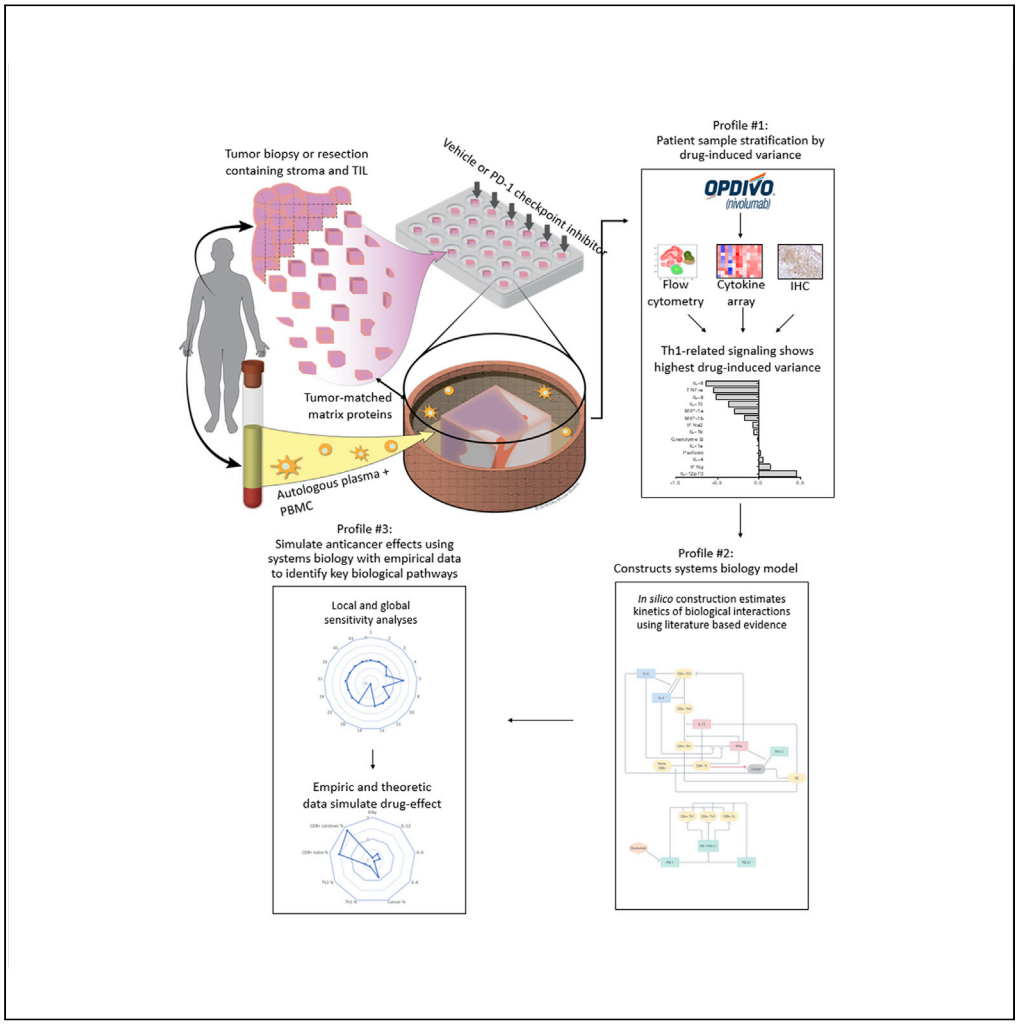

Munisha Smalley, Michelle Przedborski, Saravanan Thiyagarajan, ..., Pradip Majumder, Mohammad Kohandel, Aaron Goldman

kohandel@uwaterloo.ca (M.K.)
agoldman@bwh.harvard.edu (A.G.)

HIGHLIGHTS

Computational strategy to study anticancer immune checkpoint blockade, *ex vivo*

PD-1 blockade-induced T helper type 1 (Th1) stratifies tumor biopsies, *ex vivo*

Systems biology links drug effect to dynamic intratumor T cell proliferation

In silico sensitivity analyses of PD-1 blockade predict Th1-induced antitumor effects

Smalley et al., iScience *23*, 101229
June 26, 2020
https://doi.org/10.1016/j.isci.2020.101229

iScience

CellPress
OPEN ACCESS

Article

Integrating Systems Biology and an *Ex Vivo* Human Tumor Model Elucidates PD-1 Blockade Response Dynamics

Munisha Smalley,[1,2,3] Michelle Przedborski,[4] Saravanan Thiyagarajan,[1] Moriah Pellowe,[4] Amit Verma,[5] Nilesh Brijwani,[1] Debika Datta,[1] Misti Jain,[1] Basavaraja U. Shanthappa,[1] Vidushi Kapoor,[1] Kodaganur S. Gopinath,[6] D.C. Doval,[7] K.S. Sabitha,[8] Gaspar Taroncher-Oldenburg,[9] Biswanath Majumder,[1] Pradip Majumder,[1] Mohammad Kohandel,[4,10,*] and Aaron Goldman[2,3,10,11,*]

SUMMARY

***Ex vivo* human tumor models have emerged as promising, yet complex tools to study cancer immunotherapy response dynamics. Here, we present a strategy that integrates empirical data from an *ex vivo* human system with computational models to interpret the response dynamics of a clinically prescribed PD-1 inhibitor, nivolumab, in head and neck squamous cell carcinoma (HNSCC) biopsies (N = 50). Using biological assays, we show that drug-induced variance stratifies samples by T helper type 1 (Th1)-related pathways. We then built a systems biology network and mathematical framework of local and global sensitivity analyses to simulate and estimate antitumor phenotypes, which implicate a dynamic role for the induction of Th1-related cytokines and T cell proliferation patterns. Together, we describe a multi-disciplinary strategy to analyze and interpret the response dynamics of PD-1 blockade using heterogeneous *ex vivo* data and *in silico* simulations, which could provide researchers a powerful toolset to interrogate immune checkpoint inhibitors.**

INTRODUCTION

Cancer immunotherapies—therapies that harness the body's own immune system to fight cancer—have revolutionized cancer treatment over the past decade. A number of modalities, including immunomodulatory antibodies, adoptive immune cell transfer, and cancer vaccines have been clinically tested and brought to market. However, and despite their dramatic effect on survival rates and elimination of terminal disease in some patients, clinical success of cancer immunotherapies remains highly variable and notoriously unpredictable (Garon, 2017; Zhang and Chen, 2018). This variability and unpredictability of outcome is thought to be most likely driven by patient-specific biology (Kakimi et al., 2017; Wayteck et al., 2014), and in particular by interactions of the patient's immune system with the tumor (Spitzer et al., 2017). Predicting such interactions and studying them across heterogeneous tumors remains one of the biggest challenges in the space (Cristescu et al., 2018).

A key factor contributing to this state of affairs is a lack of well-established translational strategies and platforms that integrate inter- and intra- patient tumor heterogeneity, recapitulate cancer and stromal cell biology, recreate the tumor microenvironment and its underlying 3-dimensional architecture, and reproduce the immune compartment (Tannock and Hickman, 2016). Although current approaches to interrogate drugs, including *in vitro*, *in vivo*, and *ex vivo* preclinical models, have made great strides in addressing one or several of the above issues (Garnett et al., 2012; Samson et al., 2004; Sharma et al., 2010), most are limited by their inability to capture the full biological context of the native tumor at the individual patient level, which include the spatial arrangement of cell heterogeneity (Bertotti and Trusolino, 2013; Dhandapani and Goldman, 2017; Ruggeri et al., 2014; Samson et al., 2004). Indeed, *ex vivo* platforms are now routinely deployed to correlate empirical data with therapy response (Jahnke et al., 2014; Karekla et al., 2017; Silva et al., 2017). However, a paucity of literature has described meaningful analytical approaches to interpret intratumor immune biology with response dynamics of immune checkpoint blockade when clinical or therapy response is unknown. Indeed, such information could help

[1]Integrative Immuno-Oncology Center, Mitra Biotech, Woburn, MA, USA

[2]Department of Medicine, Harvard Medical School, Boston, MA, USA

[3]Division of Engineering in Medicine, Brigham and Women's Hospital, Boston, MA, USA

[4]University of Waterloo, Department of Applied Mathematics, Waterloo, ON N2L 3G1, Canada

[5]Max Super Speciality Hospital, New Delhi, India

[6]Bangalore Institute of Oncology, Bangalore, India

[7]Rajiv Gandhi Cancer Institute & Research Centre, New Delhi, India

[8]Kidwai Memorial Institute of Oncology, Bangalore, India

[9]Gaspar Taroncher-Oldenburg Consulting, Philadelphia, PA, USA

[10]These authors contributed equally

[11]Lead Contact

*Correspondence: kohandel@uwaterloo.ca (M.K.), agoldman@bwh.harvard.edu (A.G.)

https://doi.org/10.1016/j.isci.2020.101229

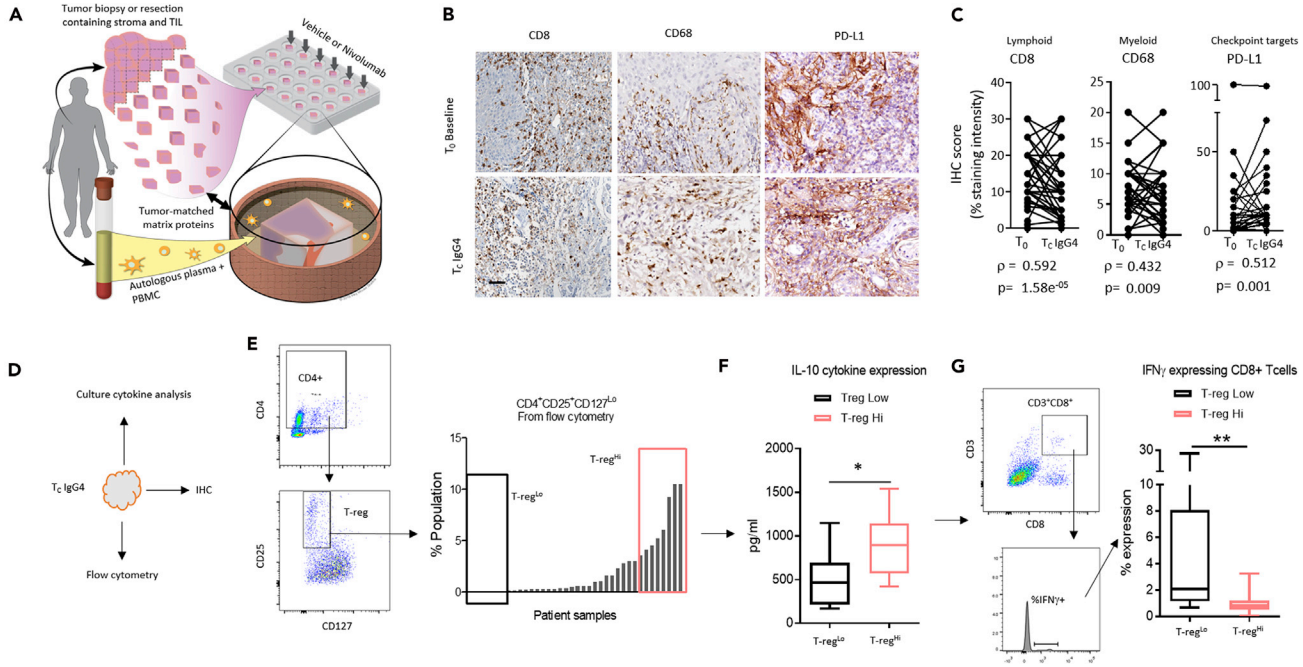

Figure 1. Profiling Spatiotemporal Immune Fidelity *Ex Vivo*, Comparing T_0 with Unstimulated Vehicle Control (T_CIgG4)

(A) Schematic of the *ex vivo* tumor model. Surgically resected or biopsied tumor tissue is obtained along with patient-matched whole blood (i.e., time 0 h, T_0). Following manual fragmentation, tissue is plated into individual tissue culture wells coated with indication- and grade-matched tumor matrix proteins along with autologous serum and peripheral blood mononuclear cells. Vehicle control or nivolumab was introduced to culture and interrogated for either 48 or 72 h (T_c). Illustration by Wendy Chadbourne, 2018, Inky Mouse Studios, www.inkymousestudios.com.

(B) Representative bright-field image from immunohistochemistry of three unique patient samples matching between T_0 and T_c. Scale bar, 40 μm.

(C) Pairwise, Spearman correlation analysis was performed using IHC pathology scores of CD8, CD68, and PD-L1 between T_0 and T_C. Spearman rho was calculated to determine correlation between the two time points. p Value <0.05 indicates the correlation is statistically significant.

(D) Schematic shows the different phenotypic response assays that are employed to study tumor phenotype and culture media during the *ex vivo* culture.

(E) Flow cytometry was used to quantify the regulatory T cell (T-reg) population in all patient tumor samples. Right panel plots the percentage of T-regs in the total population. Boxes indicate the highest and lowest T-reg expressing patient samples ($T\text{-reg}^{Hi}$ and $T\text{-reg}^{Lo}$).

(F) Box and whisker plot quantifies the IL-10 protein expression from the tissue culture media (pg/mL), determined by Luminex, in $T\text{-reg}^{Hi}$ and $T\text{-reg}^{Lo}$ patient samples (see [E]) *$p < 0.05$ by Mann-Whitney U test.

(G) Box and whisker plot shows the percent expression of IFNγ in $CD8^+$ T cells determined by flow cytometry in $T\text{-reg}^{Hi}$ and $T\text{-reg}^{Lo}$ patient samples, which were grouped from (E), **$p < 0.01$ by Mann-Whitney U test.

See also Figure S1 contains patient demographic data.

fuel interrogation strategies and advance programs for pre-clinical investigation of cancer immunotherapy, such as checkpoint inhibitors.

We previously described a multi-compartment *ex vivo* platform, which preserves the cellular architecture and heterogeneity of solid tumors with a high degree of morphologic and kinase signaling fidelity (Majumder et al., 2015). The platform incorporates autologous peripheral constituents including immune cells and the patient's autologous plasma, which are explanted into a culture well containing tumor matrix proteins that match the grade or stage, and indication of each tumor type. To this, anticancer drugs are introduced to the co-culture for up to 3 days (Figure 1A). The utility of this platform for interrogating the biology of emerging cancer immunotherapies has yet to be tested, which requires interrogation of the immune compartment including a compatible and comprehensive analytical strategy to interpret the data.

Nivolumab (Opdivo) is one of two predominant US Food and Drug Administration-approved immune checkpoint inhibitors that targets programmed cell death protein 1 (PD-1). Pharmacodynamics (response dynamics) of PD-1 inhibitors are poorly understood, and therapy response to PD-1 inhibitors vary dramatically from patient to patient. The most widely explored biomarkers for predicting responders to PD-1 inhibitors are the expression level of programmed death-ligand 1 (PD-L1) and tumor mutational burden (TMB), which track to overall clinical response rates of 27% and 58%, respectively (Ferris et al., 2018; Goodman et al., 2017). Despite these advances,

PD-1 inhibitors are still prescribed for patients with low or negative PD-L1 levels or low TMB because positive clinical benefit to anti-PD-1 drugs remain better when compared with chemotherapy (Ferris et al., 2018; Goodman et al., 2017). It is increasingly clear that a robust approach to study and interpret response dynamics of immune checkpoint inhibitors using completely human models may shift the course of drug development and our understanding for the mechanisms that confer response or resistance in the clinic.

Here, we describe a multi-pronged strategy to interrogate the response dynamics of the PD-1 checkpoint inhibitor, nivolumab, using our *ex vivo* system with human head and neck squamous cell carcinoma (HNSCC) biopsies (N = 50) where actual clinical response is unknown. First, we explored the fidelity of the platform for interrogating immuno-oncology drugs by establishing spatial distribution of immune cells and functional tumor-immune biology over the course of culture and examined these features across the lymphoid and myeloid compartments. Second, we describe a stratification method that considers patient-wide heterogeneity integrating drug-induced variance to compare the effect of nivolumab in subgroups of tumor samples with shared response dynamic profiles. Third and finally, we describe the use of a systems biology framework and mathematical simulations of local and global sensitivities to estimate the contribution of starting and drug-induced values from the empirical data as they impact "anti-tumor" effects. The approach outlined here provides both an unbiased picture for the downstream effects of PD-1 checkpoint blockade and an interdisciplinary analytical methodology to interrogate response dynamics from heterogeneous *ex vivo* data, which could be applied to other similar pre-clinical cancer immunotherapy models.

RESULTS

Testing for Preservation of the Tumor-Immune Contexture, *Ex Vivo*, across Multiple Biological Assays

We deployed an *ex vivo* tumor culture system comprising live tissue fragments, which contain intact tumor, stroma, and infiltrated immune cells, as well as patient-autologous peripheral immune cells supplied in the culture media with plasma ligands (Figure 1A). We hypothesized that this system would provide a suitable substrate to interrogate rapidly induced intratumor response dynamics of immune checkpoint inhibitors. To test this hypothesis, we first explored fidelity of the tumor-immune contexture during *ex vivo* culture in unstimulated conditions (IgG4 vehicle control). We obtained tumor samples from patients with advanced and late stage HNSCC (Figure S1) and tested preservation of the tumor-immune microenvironment. Primarily, we examined retention of protein expression patterns, as well as lymphocyte infiltration and spatial heterogeneity between T_0, which is defined as the time when the tumor arrives at the laboratory (24–36 h from resection or biopsy in the clinic), and T_C, which is defined as the period 48–72 h after *ex vivo* culture. In this case, T_C is in the absence of exogenous stimuli (i.e., IgG4 control). First, we tested for retention of tumor-resident T-cells (CD8), macrophages (CD68), and tumor markers, such as PD-L1 over the course of the *ex vivo* culture. Using immunohistochemistry (IHC) and pathology scoring, we determined there was a high degree of concordance between T_0 and T_C during culture, indicated by Spearman correlation (Figures 1B and 1C). In confirmation of these data, we analyzed tissue fragments by flow cytometry (Figure S2A) and quantified spatial arrangement of lymphocytes in the tumor versus stroma at both T_0 and T_C, detecting a similar degree of preservation (Figures S2B–S2D).

Next, we deployed multiple biological assays including flow cytometry of tumor tissue fragments, multiplex cytokine analysis of the tissue culture supernatant, and IHC to ask whether expected biological networks were retained post culture. First, as a cross-technology validation, we confirmed that expression of CD8 in IHC overlapped with the expression patterns of CD8 in flow cytometry from the same patient samples (quantified as deviation from the mean), suggesting consistency across different assays performed (Figures S3A and S3B). Next, we segregated patient samples based on expression levels of Foxp3 from IHC, a biomarker of immune suppressive T-reg cells, separating samples into two cohorts: high-expressing ($Foxp3^{Hi}$) and low-expressing ($Foxp3^{Lo}$). We confirmed cohort membership by showing the $Foxp3^{Hi}$ subset contained significantly more $Foxp3^{+}$ T-reg cells compared with the $Foxp3^{Lo}$ cohort ($p < 0.05$) as determined by a different biological assay, flow cytometry (Figures S3C and S3D).

Finally, we tested whether we could recapitulate *in vivo* signaling mechanisms that contribute to lymphocyte lineage differentiation. For example, microenvironments enriched for T-reg cells are also enriched for IL-10 cytokines and often inversely correlate to the abundance of IFNγ+ CD8+ T cells (Saraiva and O'Garra, 2010). We used flow cytometry to first segregate the biopsies into two cohorts—high T-reg ($T\text{-reg}^{Hi}$) and low T-reg ($T\text{-reg}^{Lo}$) abundance—based on $CD4^{Hi}$, $CD25^{Hi}$, and $CD127^{Lo}$ expression (Figures 1D and 1E).

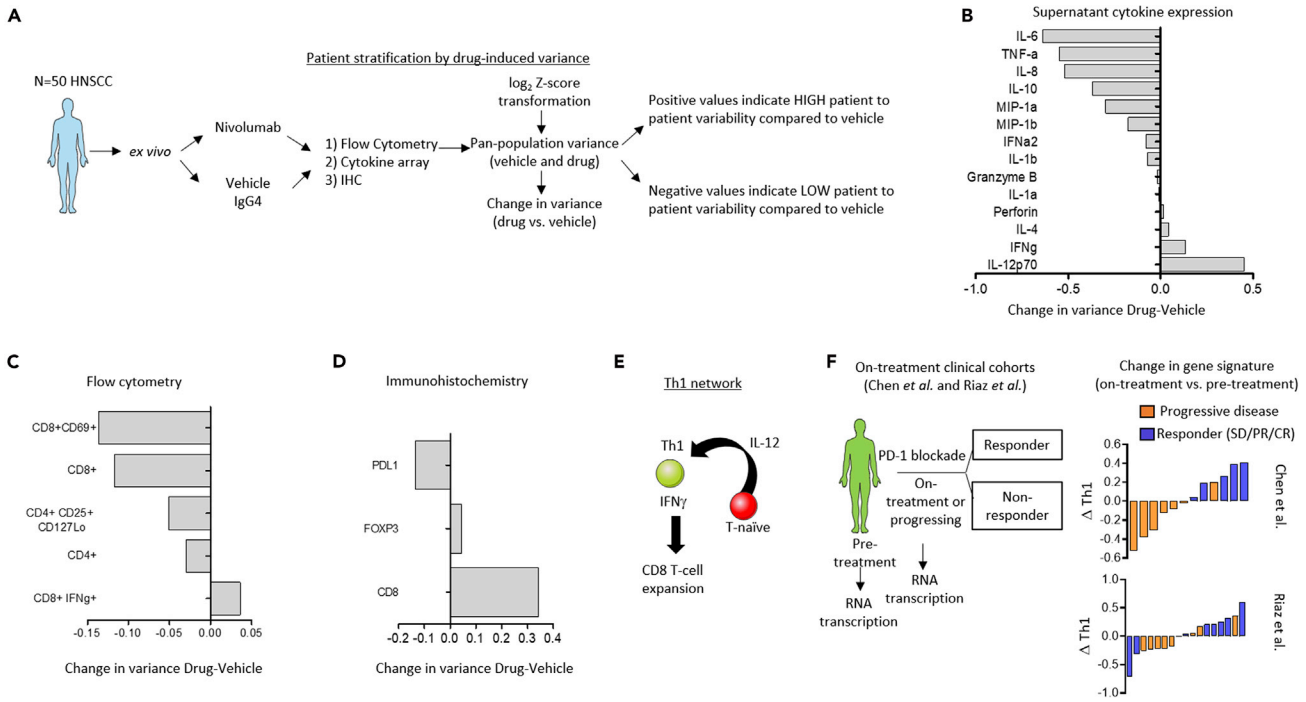

Figure 2. Drug-Induced Patient Variance as a Method to Stratify Heterogeneous Samples Pin Points a Role for the Th1-Related Pathway

(A) Schematic shows analysis workflow to determine drug-induced variance.

(B–D) Waterfall plots show the change in variance of cytokines, and gene and protein immune cell signatures in the vehicle control versus drug pressure from NanoString (A), flow cytometry (B), cytokine profiling (C), and immunohistochemistry (D). Calculation for variance can be found in the Transparent Methods section. Positive values indicate protein expressions that are more variable from patient to patient under nivolumab pressure compared with the vehicle control, i.e., the drug has the effect of creating high degree of phenotypic heterogeneity across all the patient samples. Negative values indicate those proteins signatures that are less variable across all patient samples under nivolumab pressure compared with the vehicle control, i.e., nivolumab has the effect of normalizing phenotype across patient samples relative to the vehicle.

(E) Schematic shows the clinical study reported in Chen et al. and Riaz et al.

(F) Waterfall plots show the measurable change of Th1 gene transcription signature in data obtained from Chen et al. and Riaz et al.

We confirmed the relationship between IL-10 expression and T-reg abundance, which was significantly higher in the culture supernatant of T-reg^{Hi} tumor samples than in the T-reg^{Lo} ones ($p < 0.05$) (Figure 1F). As expected, IFNγ+ CD8+ T cells were significantly lower in the T-reg^{Hi} tumor samples than in the T-reg^{Lo} ones (Figures 1F and 1G). Taken together, these data describe the level to which the *ex vivo* tumor culture preserves the tumor-immune contexture including biological networks and cross-assay fidelity.

PD-1 Blockade-Induced Variance Identifies T Helper Type 1 as Conferring the Greatest Impact on Patient-to-Patient Heterogeneity

Ex vivo human tumor models pose a unique challenge because of the interpatient and intratumor heterogeneity. Thus, interpreting the data from *ex vivo* and organoid clinical explant models in the context of cancer immunotherapies remains a major challenge in cancer research (Dhandapani and Goldman, 2017; Maciejko et al., 2017).

Given the range and diversity of phenotypes and drug-induced effects, we sought to deploy a method of stratifying the heterogeneous patient samples into smaller cohorts based on drug effect. To do this, we performed a variance calculation for control and treatment groups to detect the change in variance of protein expression patterns between samples after drug pressure. Data were transformed to $\log_2$ Z-scores to obtain mean of 0 and standard deviation of 1. The variance across all patient samples for each biomarker or signature within a treatment was calculated and vehicle variance was subtracted to obtain the change in variance. Using this method, we could determine whether the drug had a large impact on patient-to-patient response heterogeneity (i.e., positive change in variance) or whether the drug had little to no impact across patient samples compared with the vehicle control vis-á-vis a negative change in variance (Figure 2A). Using this strategy we determined that PD-1 blockade induced a high degree of interpatient

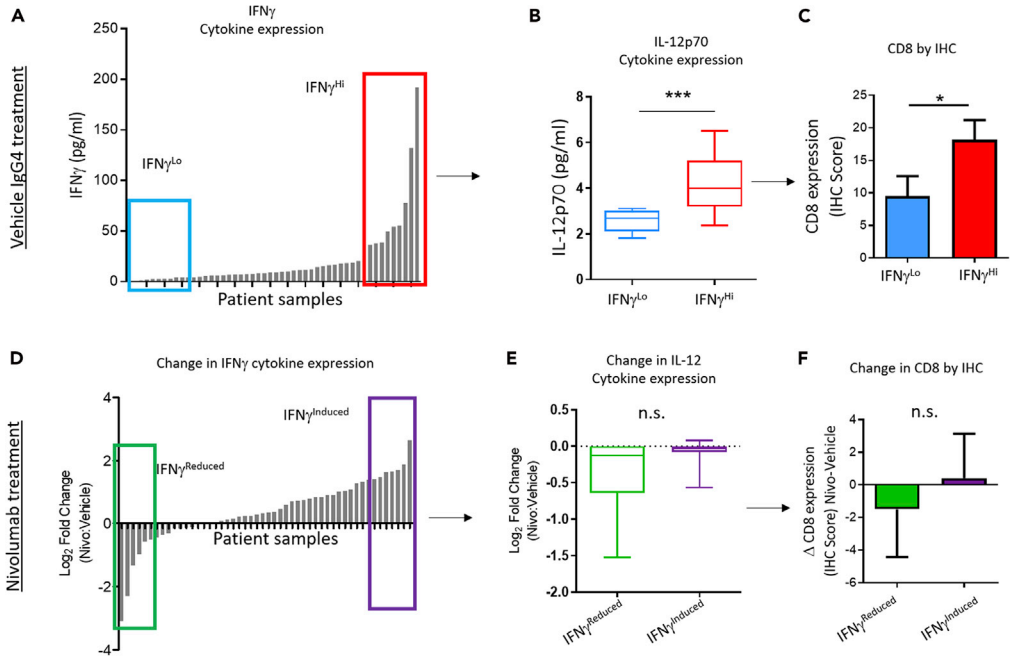

Figure 3. Th-1 Related Pathway Is Not Simultaneously Activated under Drug Pressure, *Ex Vivo*

(A) Histogram shows IFNγ concentration (pg/mL) in the culture supernatant from the vehicle-treated cohort of all 50 patient samples determined as a mean expression at 24, 48, and 72 h culture. Boxes indicate patient samples that are stratified into the highest and lowest IFNγ expression ($IFN\gamma^{HI}$ and $IFN\gamma^{Lo}$).

(B) Box plot shows IL-12p70 cytokine concentration in the culture media of $IFN\gamma^{HI}$ and $IFN\gamma^{Lo}$ cohorts, ***$p < 0.001$ by Mann-Whitney U test.

(C) Histogram shows expression of CD8 in tumor tissue of $IFN\gamma^{HI}$ and $IFN\gamma^{Lo}$ cohorts determined by IHC, *$p < 0.05$ by Mann-Whitney U test.

(D) Waterfall plot shows $\log_2$ fold change in IFNγ concentration in culture media comparing nivolumab with vehicle IgG4. Colored boxes indicate the patient samples with the largest increase and decrease in IFNγ expression after PD-1 drug exposure ($IFN\gamma^{Induced}$ and $IFN\gamma^{Reduced}$, respectively).

(E) Box plot shows IL-12p70 cytokine concentration in the culture media of $IFN\gamma^{Induced}$ and $IFN\gamma^{Reduced}$ cohorts, n.s. indicates sample sets are not significantly different by Mann-Whitney U test.

(F) Histogram shows expression of CD8 in tumor tissue of $IFN\gamma^{Induced}$ and $IFN\gamma^{Reduced}$ cohorts determined by IHC, n.s. indicates sample sets are not significantly different by Mann-Whitney U test.

heterogeneity in T helper type 1 (Th1)-related pathways indicated by the positive change in variance of IFNγ and IL-12 (Athie-Morales et al., 2004) cytokine expression levels and $CD8^+$ $IFN\gamma^+$ T cells (Ekkens et al., 2007) analyzed by flow cytometry, which was confirmed by IHC for CD8 (positive change in variance compared with the vehicle IgG4 control) (Figures 2B–2E).

To provide a translational impact to these findings, we obtained gene expression data from patients biopsied before treatment or while on-treatment, of PD-1 checkpoint therapy (Chen et al., 2016; Riaz et al., 2017) (Figure 2F) and examined Th1 gene expression profiles in the clinical dataset. We determined that a shift in the expression of Th1-related genes associated with better clinical response, as evidenced by the change in Th1 gene expression *Z* score in the waterfall plot (Figure 2F). Although this finding was expected, it supports the hypothesis that patient-to-patient drug-induced variability observed *ex vivo*, primarily in the expression of Th1-related phenotypes, may be a reasonable approach to stratify the heterogeneous *ex vivo* samples and study response dynamic profiles of the diverging subgroups, which may provide some information for features of "response" versus "resistance."

To this end, we asked whether expected biological pathways in the Th1 pathway were conserved or perturbed; we determined that, although expected biological networks, such as IFNγ, IL-12, and Th1 signaling cascade (Athie-Morales et al., 2004; Kieper et al., 2001) are retained in the vehicle control cohort (Figures 3A–3C), these same biological networks could not be recapitulated, or reasonably

"linked together" after PD-1 blockade (Figures 3D–3F), which suggested that some biological mechanisms may not be able to be captured *ex vivo* in such a short culture period (i.e., up to 72 h) and therefore a more unbiased approach to stratify and study response dynamics should be employed for heterogeneous datasets.

In Silico Simulation Implicates Dynamic Th1-Related Molecular Pathways in the Anticancer Effects of PD-1 Blockade

A major advance in the pre-clinical study of cancer immunotherapies is the integration of response dynamics with antitumor effects. Here, and in the absence of matched-patient clinical information, we wanted to infer how drug-induced response dynamics may link to putative anticancer effects of PD-1 blockade. We integrated the empirical *ex vivo* data, including initial starting concentrations and the dynamic range and changes of different Th1-related cell types and cytokines, into an *in silico* model. First, we developed a systems biology network comprising a tumor cell population along with five key interacting T cell populations and four key cytokines involved in T helper cell differentiation and activation (Figure 4). We then performed numerical simulations to investigate the sensitivity of the model's response to initial conditions and parameter values. The model consisted of 17 coupled ordinary differential equations (ODEs), which describe the time evolution of the cytokine concentrations, T cell populations, tumor cell population, and PD1 and PD-L1 levels (and the interaction of the latter with nivolumab). The 17 ODEs were parameterized by 47 distinct kinetic parameters (Supplemental Information). Summarized by the schematic in Figure 5, we then developed simulations of local and global sensitivity analysis to infer the effect of PD-1 blockade, the role of Th1-related cytokines and cell markers, and antitumor phenotypes. To do this, we used the *ex vivo* data in the context of nivolumab to determine the values of the model parameters, which was done by setting the initial T cell populations to the average of all patients (vehicle IgG4) and by setting the initial cytokine levels to values within the range of average $\pm$ SD of all patients (vehicle IgG4). Then, we integrated the nivolumab-treated cytokine data at the 24-h intervals (72 h total culture) and the T cell populations from flow cytometry to develop both a local and global sensitivity analysis (Supplemental Information).

Local sensitivity analysis was then conducted around the nominal parameter set to determine how small perturbations to the parameter values affect the strength of the response (defined as the increased assumed death of cancer cells) to treatment with nivolumab by varying one parameter at a time. The resulting relative sensitivities indicated that the efficiency of cytotoxic T cells at killing cancer cells (parameter 14), as well as kinetic parameters related to the proliferation rate of the cancer cells and the CD8+ cytotoxic T cells (parameters 4, 5, and 8), had the highest sensitivities and thus the largest effect on the strength of the response to treatment (Figures 6A and 6B). In the radial plots, a higher sensitivity value is indicated by a larger distance from the origin (center of the plot). Thus, as Figure 6A shows, most of the parameters corresponded to a small sensitivity value, except for those emphasized above.

Although small perturbations to single kinetic parameters affected the strength of the response to treatment, they were not enough to change the nature of the response to the treatment. Thus, we next performed global sensitivity analysis, which involved randomly changing all the initial cytokine levels and/or initial T cell populations and/or values of the kinetic parameters of the model simultaneously.

We determined that varying all the initial protein levels was not sufficient to induce a "non-response" phenotype; however, the strength of the response to treatment (as indicated by the final cancer cell population size) showed a power-law dependence on the initial IL-12 level of the form $\tilde{C}_{72} \propto [\mathrm{IL}-12]^{-\beta}$, $\beta > 0$, where $\tilde{C}_{72}$ is the size of the cancer cell population at t = 72 h. In the model, the production of Th1 cells is dependent on IL-12 levels, which indicates that, as observed experimentally, an increase in Th1 levels may correlate with a stronger response to treatment. To investigate this point further, we kept the kinetic parameters, initial protein levels, and initial relative T cell populations fixed at their nominal values and varied only the initial cancer population level. We found that, when the initial cancer cell population comprises less than approximately 75% of the tumor biopsy, increased Th1 levels correlate with stronger treatment response. This trend is likely driven by the production of IL-12 by dendritic cells, which are assumed to be proportional to the cancer cell population. However, when the initial cancer population level exceeds more than approximately 75% of the tumor biopsy, the complex interplay between Th1 and Th2 cytokines produced by the cancer cells ultimately leads to decreasing response to treatment, despite increasing Th1 levels (Figure 6C, right side of the dashed vertical line).

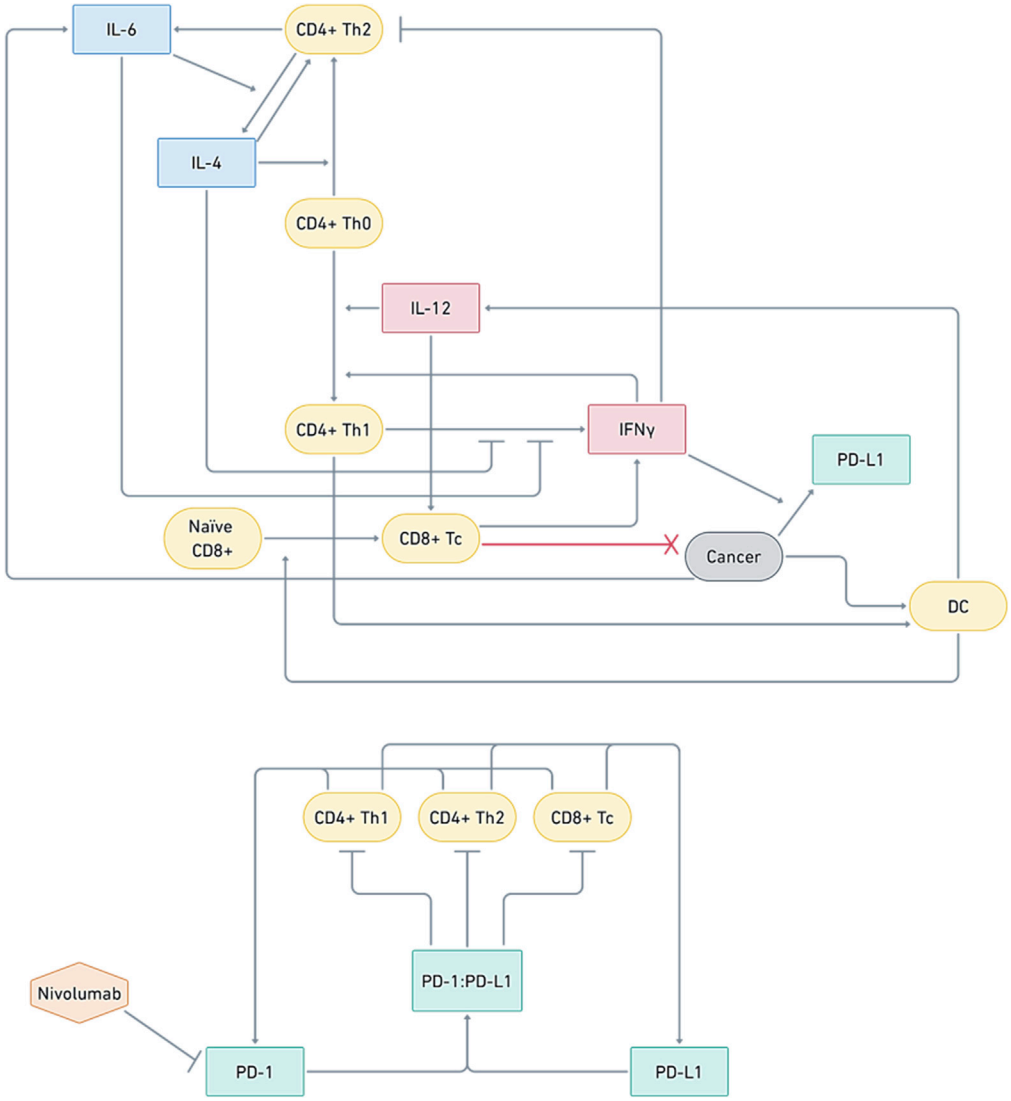

Figure 4. Systems and *In Silico* Strategy to Study Th1-Related Phenotypes in the PD-1/PD-L1 Network

Systems biology model, illustrating interactions between cell populations, cytokines, and PD-1 and PD-L1. Naive CD4+ T helper cells (Th0) differentiate into CD4+ Th1 or CD4+ Th2 cells, which is influenced by Th1 cytokines (IL-12 and IFNγ) and Th2 cytokines (IL-4, IL-6). CD4+ Th1 cells influence the differentiation of naive CD8+ cells into CD8+ cytotoxic (Tc) T cells, which kill cancer cells. Cancer cells express PD-L1, which can bind to PD-1 expressed by CD4+ Th1, CD4+ Th2, and CD8+ Tc cells, thus inhibiting them.

Although changing the initial proportion of cancer cells comprising the biopsy affected the strength of the response to treatment, it did not induce a non-response phenotype for the nominal parameter set, even when the initial cancer population comprised up to 90% of the tumor cell population. To induce a non-response phenotype, it was necessary to change the initial relative T cell populations. In particular, by varying both the initial protein levels and initial relative T cell populations, while keeping all other parameters fixed at their nominal values, we could induce a simulated non-response phenotype. In this way, we found that the size of the cancer cell population at t = 72 h showed the highest sensitivity to the initial CD8+ cytotoxic T cell level, followed by the initial naive CD8+ T cell level (Figure 6D).

Finally, in an attempt to capture the heterogeneity in patient tumor microenvironment and response to treatment, we varied all the kinetic parameters, initial cytokine and PD-L1 levels, and initial T cell levels simultaneously. We used multi-parametric sensitivity analysis (MPSA) (Cho et al., 2003; Hornberger and

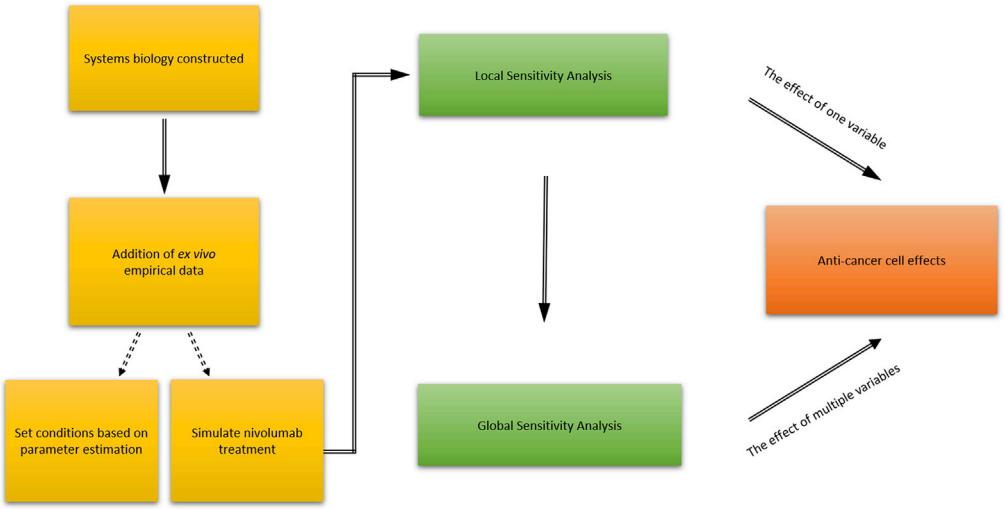

Figure 5. Integrating *Ex Vivo* Data into *In Silico* Analysis

Schematic showing the procedure to integrate nivolumab-treated *ex vivo* empirical evidences *in silico* for local and global sensitivity analyses.

Spear, 1981; Zi et al., 2005), which evaluates the parameter (and initial condition) sensitivities based on Kolmogorov-Smirnov statistics, returning sensitivity values between 0 and 1. A larger parameter sensitivity indicates that the corresponding parameter variation has a large impact on the model output (Zi, 2011). The results are presented in Figures 6E and 6F. Based on the MPSA sensitivities, the treatment response is most sensitive to the following kinetic parameters and initial conditions: the efficiency of cytotoxic T cells at killing cancer cells (parameter 14), the initial cytotoxic CD8+ T cell level, the rate of production of IFNγ by cytotoxic T cells (parameter 47), the initial naive CD8+ T cell level, the IL-4-independent growth rate of Th2 cells (parameter 6), the net proliferation rate of Th1 cells (parameter 3), the initial IL-6 level, and the half-maximal IFNγ concentration for IFNγ-dependent differentiation of naive CD4+ T cells into Th1 cells (parameter 25). These results reinforce the experimental observation that the variability in patient response is connected to the upregulation of Th1 levels.

Taken together, we report the integration of biological and mathematical strategies to interpret the response dynamics of PD-1 blockade in heterogeneous solid human tumor biopsies where matched-patient clinical information is missing. This approach took into consideration biological fidelity of the *ex vivo* system, methods of stratifying samples to identify drug-induced variability and systems biology approaches that can subsequently simulate key pathways contributing to antitumor phenotypes.

DISCUSSION

Predicting clinical response to therapy is a "holy grail" in the quest for durable, sustainable cures for cancer. Numerous preclinical and translational methods, including *in vitro* and *ex vivo* models, have been developed in the past decade to help guide our understanding for the clinical activity of immunotherapy (Jenkins et al., 2018; Meijer et al., 2017). Indeed, syngeneic animal models, which contain a full immune complex, are used to study cancer immunotherapies in a pre-clinical context, yet they often fall short in recreating the human response to drugs and immunotherapies as they lack critical lymphocytes (Day et al., 2015). Organotypic tumor spheroid models, on the other hand, recreate murine drug responses (Jenkins et al., 2018). Indeed, three of the most important aspects of assessing drug response in immunotherapy have been recently suggested as (1) the native spatial arrangement of the immune cells (Yuan, 2016), (2) autologous factors to recreate the host environment (Dhandapani and Goldman, 2017; Jackson and Thomas, 2017), and (3) clinically relevant integration of data to correlate response dynamics with predicted success or failure of a drug (Meijer et al., 2017). However, there remains a limited understanding for the biological and translational interpretations of data arising from *ex vivo* cancer immunotherapy models. To this end, our work provides a methodology to study adaptive immune responses using multiple biological and computational approaches, which elucidate pathways and signatures at the protein level. *Ex vivo* tumor systems in collaboration with systems biology and computational models could

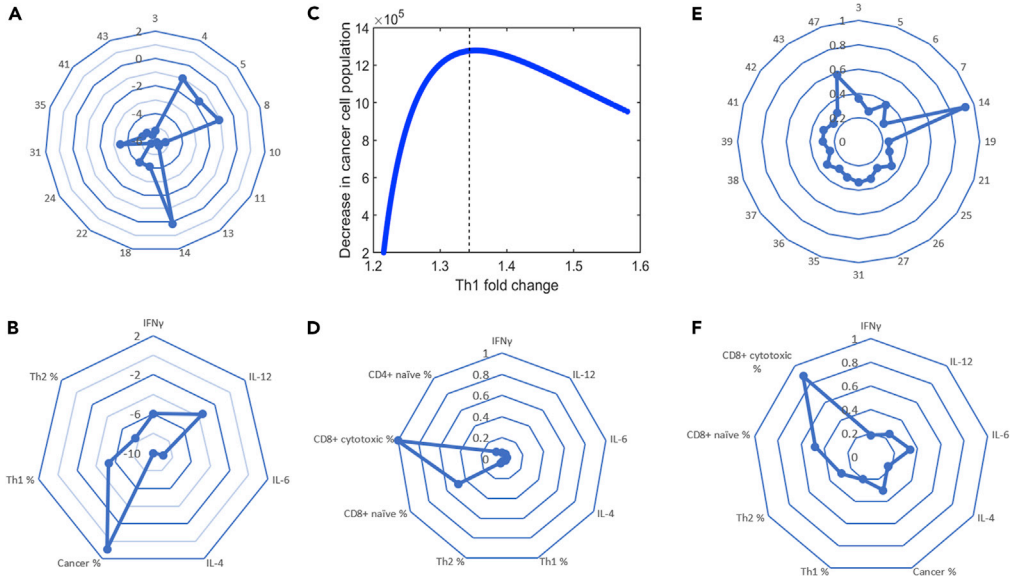

Figure 6. Local Sensitivity Analyses (LSA) and Global Sensitivity Analyses (GSA) Integrate Th1-Related Phenotypes to Simulate Antitumor Effect of PD-1 Blockade

(A) Relative sensitivities determined by LSA for the top 15 kinetic parameters (indicated by parameter number).

(B) Relative sensitivities determined by LSA for initial cytokine levels and initial T cell populations. For (A) and (B), the Log_{10} of the absolute value of the relative sensitivities are presented for visual clarity.

(C) Decrease in cancer cell population at t = 72 h with PD-1 blockade as a function of Th1 induction, obtained by changing only the initial cancer cell population. Initial cancer cell population comprises less than 75% of the tumor for points to the left of the dashed vertical line.

(D) MPSA sensitivities determined by GSA for the initial protein levels and initial relative T cell populations.

(E) MPSA sensitivities determined by GSA for the top 20 kinetic parameters (indicated by parameter number).

(F) MPSA sensitivities determined by GSA for the initial cytokine levels and T cell populations. In (E) and (F), all protein levels, initial T cell populations, initial cancer cell population, and kinetic parameters were varied.

therefore be a powerful toolset to investigate and understand "dynamic drug response" of human tumors.

Here, we described an analytical approach that leverages an *ex vivo* model to study phenotypic "reflex" to anticancer immune checkpoint inhibitors. Importantly, we described preservation of the spatial tumor-immune contexture and conservation for the complex signaling networks between immune and tumor cells using autologous factors, which are unique to each patient. One question that remains open is the role that systemic lymphocytes (i.e., PBMCs) contribute to the *ex vivo* culture system. In a separate set of experiments using breast cancer samples, we determined that PBMCs will infiltrate the tumor fragment at a rate of 1%–2% of the total tumor CD45+ population, which becomes more variable when PD-1 checkpoint inhibitors are added (data not shown). This observation leads us to the conclusion that PBMCs may influence the spatial arrangement of immune cells in the tumor fragment and alter the immunobiology in response to PD-1 blockade. Indeed, in the present study induction of T helper cells, particularly Th1, was a putative indication for the conversion of an immune-deficient tumor into one that exhibited multiple inflammation-like features, including induction of pro-inflammatory cytokines. A more complete interrogation, in a separate study, is worthwhile in order to understand how exogenous immune cells influence the drug response, *ex vivo*.

Identifying checkpoint inhibitor-induced cell death in human *ex vivo* models is undescribed and remains a challenge in this space. In a study published by Jenkins et al., they used mouse-derived organotypic tumor spheroids (MDOTS), showing that immune-mediated cell death can be observed in a time frame of 5–6 days (Jenkins et al., 2018). However, in the same study, the observations were not recapitulated in a similar time frame using patient-derived organotypic tumor spheroids (PDOTS). Interestingly, Jenkins et al. described a change in the immune biology after exposure to PD-1 inhibitors, vis-á-vis changes to the cytokine expression profile within 72 h. This is not different from our findings. Indeed, we demonstrate that, in the absence of obvious cell death signals after treatment with PD-1 blockade in human samples, we do

observe changes to the immune biology. Importantly, we demonstrate, for the first time, how this information can be leveraged with computational models to estimate the antitumor effects *in vivo*. Such an approach could help researchers understand anticancer effects of immunotherapy, leveraging changes to the immunobiology in the absence of obvious cell death markers.

Translational tools that recapitulate the human microenvironment are urgently needed to advance cancer research and drug development, particularly in the era of immunotherapy (Dhandapani and Goldman, 2017; Jackson and Thomas, 2017). While interrogating the effect of PD-1 blockade, we used an unbiased approach to dissect the response dynamics to PD-1 inhibition. Our expectation that we would be able to link known biological pathways to one another under drug pressure (e.g., IFNγ, IL-12, CD8+ T cell expansion) was thwarted when we applied nivolumab and attempted to elucidate molecular biology via IFNγ induction. Instead, we concluded that, although established biological mechanisms are preserved in the vehicle control groups, interpatient heterogeneity—and likely also the result of time in culture—confounded our ability to recapitulate known lymphocyte lineage differentiations and signaling relationships. For this reason, we determined that a more useful strategy was to examine drug-induced changes in variance across patient samples and use that information to guide a response dynamics approach, first. Subsequently, features of response and resistance could be bridged with response dynamics and drug-induced interpatient heterogeneity using variance of immune markers. In taking such an unbiased, integrative approach we successfully recapitulated biological features that have been previously described in the literature (e.g., acute phase reaction cytokines and induction of Th1-associated genes).

To estimate the anticancer effects of PD-1 blockade based on changes to immunobiology, we integrated the empirical *ex vivo* data into an *in silico* model. We first determined a set of nominal parameter values to match the average patient data, then we performed local and global sensitivity analysis to elucidate the parameters that were most important for influencing the treatment response. We found that local sensitivity analysis, in which the parameters are perturbed *individually* by small values around one parameter set, did not capture the variability in the untreated patient data. Since biological model inputs such as kinetic parameters and initial concentrations are thought to vary within a large range in different cell types and cellular environments (Zi, 2011), and are therefore expected to be highly variable between patients, it was necessary to vary several parameters simultaneously to capture the experimentally observed variability in treatment response. Importantly, in doing so, the *in silico* model reproduced the experimental observation that Th1 induction correlated with increased treatment response (under certain initial conditions). It should be noted that, although these results agree with experimental observations, only a subset of immune cell populations were included in the model and several simplifying assumptions were made to reduce the complexity of the model. In future work, we will relax some of these assumptions and include additional cytokines and immune cell populations and investigate potential resistance mechanisms to PD-1 blockade. Overall, these *in silico* data demonstrate the complexity of response dynamic changes that occur under nivolumab pressure, thus emphasizing the need for integrating multiple parameters profiled in an *ex vivo* model to inform the effect of immunotherapy intervention.

Limitations of the Study

Further prospective evaluation is necessary. For instance, human papillomavirus (HPV) positivity in patients with HNSCC has been shown to correlate with a survival advantage (Benson et al., 2014). The HPV status of the HNSCC samples in this study is unknown, but HPV infections have been described at relatively low frequency in the same demographic population that our samples were obtained (Southern India) (Bandhary et al., 2018). If known, HPV status could allow for a better segregation and understanding of PD-1 blockade response dynamics. In addition, our evidence that spatial heterogeneity can provide unique information about the drug response role of CD4+ and CD8+ T cells could be expanded to understand their localization within the tumor. For example, intratumoral and stromal lymphocyte heterogeneity could provide functional information in the context of other solid tumors such as breast (Mani et al., 2016). Future studies that integrate these types of analytical features, which can be associated with the same patient's response in the clinic, could provide novel information about the behavior of patient-specific response to PD-1 blockade.

Resource Availability

Lead Contact

Further information and requests for resources, additional data and reagents should be directed to and will be fulfilled by the Lead Contact: Dr. Aaron Goldman (agoldman@bwh.harvard.edu).

Materials Availability

New materials were not generated in the course of this study.

Data and Code Availability

Code related to simulated treatment protocols for the *ex vivo* experiments with specified inputs and outputs, as well as comments throughout the code, can be found at https://github.com/mprzedborski/ex-vivo-PD1-blockade. Raw data used for analysis and simulations will be available upon request.

METHODS

All methods can be found in the accompanying Transparent Methods supplemental file.

SUPPLEMENTAL INFORMATION

Supplemental Information can be found online at https://doi.org/10.1016/j.isci.2020.101229.

ACKNOWLEDGMENTS

A.G. is funded by a Breast Cancer Alliance Young Investigator Award. M.K. and M. Przedborski. acknowledge the financial support from the Canadian Institutes of Health Research (CIHR).

AUTHOR CONTRIBUTIONS

M.S., S.T., and A.G. conceived the study and experimental design, analyzed data, and interpreted the results. M. Przedborski, M. Pellowe, and M.K. designed mathematical models, performed *in silico* simulations, analyzed the data, and interpreted the results. P.M. was responsible for oversight of *ex vivo* tissue culture experiments. M.S., S.T., N.B., M.J., D.D., and B.M. performed experiments. B.U.S. performed immunohistochemistry experiments. V.P. analyzed gene expression data from the literature. K.S.G., D.C.D., and K.S.S. provided clinical samples and helped craft the manuscript. A.G., M.S., M. Przedborski, and G.T.-O. wrote the manuscript.

DECLARATION OF INTERESTS

S.T., B.M., P.M., A.G., M.S., M.J., B.U.S., V.K., D.D., N.B., and G.T.-O. declare conflicts of interest as employees or consultants and/or holding equity in Mitra Biotech. All other authors declare no conflicts of interest. Patent applications have been filed by Mitra Biotech on behalf of authors A.G., B.M., and P.M. related to the research in this study.

Received: January 6, 2020
Revised: April 1, 2020
Accepted: May 29, 2020
Published: June 26, 2020

REFERENCES

Athie-Morales, V., Smits, H.H., Cantrell, D.A., and Hilkens, C.M. (2004). Sustained IL-12 signaling is required for Th1 development. J. Immunol. *172*, 61–69.

Bandhary, S.K., Shetty, V., Saldanha, M., Gatti, P., Devegowda, D., Pushkal, S.R., and Shetty, A.K. (2018). Detection of human papilloma virus and risk factors among patients with head and neck squamous cell carcinoma attending a Tertiary Referral Centre in South India. Asian Pac. J. Cancer Prev. *19*, 1325–1330.

Benson, E., Li, R., Eisele, D., and Fakhry, C. (2014). The clinical impact of HPV tumor status upon head and neck squamous cell carcinomas. Oral Oncol. *50*, 565–574.

Bertotti, A., and Trusolino, L. (2013). From bench to bedside: does preclinical practice in translational oncology need some rebuilding? J. Natl. Cancer Inst. *105*, 1426–1427.

Chen, P.L., Roh, W., Reuben, A., Cooper, Z.A., Spencer, C.N., Prieto, P.A., Miller, J.P., Bassett, R.L., Gopalakrishnan, V., Wani, K., et al. (2016). Analysis of immune signatures in longitudinal tumor samples yields insight into biomarkers of response and mechanisms of resistance to immune checkpoint blockade. Cancer Discov. *6*, 827–837.

Cho, K.H., Shin, S.Y., Kolch, W., and Wolkenhauer, O. (2003). Experimental design in systems biology based on parameter sensitivity analysis using a Monte Carlo method: a case study for the TNF alpha-mediated NF-kappaB signal transduction pathway. Simulation *79*, 726–739.

Cristescu, R., Mogg, R., Ayers, M., Albright, A., Murphy, E., Yearley, J., Sher, X., Liu, X.Q., Lu, H., Nebozhyn, M., et al. (2018). Pan-tumor genomic biomarkers for PD-1 checkpoint blockade-based immunotherapy. Science *362*, eaar3593.

Day, C.P., Merlino, G., and Van Dyke, T. (2015). Preclinical mouse cancer models: a maze of opportunities and challenges. Cell *163*, 39–53.

Dhandapani, M., and Goldman, A. (2017). Preclinical cancer models and biomarkers for drug development: new technologies and emerging tools. J. Mol. Biomark. Diagn. *8*, 356.

Ekkens, M.J., Shedlock, D.J., Jung, E., Troy, A., Pearce, E.L., Shen, H., and Pearce, E.J. (2007). Th1 and Th2 cells help CD8 T-cell responses. Infect. Immun. *75*, 2291–2296.

Ferris, R.L., Blumenschein, G., Jr., Fayette, J., Guigay, J., Colevas, A.D., Licitra, L., Harrington, K.J., Kasper, S., Vokes, E.E., Even, C., et al. (2018). Nivolumab vs investigator's choice in recurrent or metastatic squamous cell carcinoma of the head and neck: 2-year long-term survival update of CheckMate 141 with analyses by tumor PD-L1 expression. Oral Oncol. *81*, 45–51.

Garnett, M.J., Edelman, E.J., Heidorn, S.J., Greenman, C.D., Dastur, A., Lau, K.W., Greninger, P., Thompson, I.R., Luo, X., Soares, J., et al. (2012). Systematic identification of genomic markers of drug sensitivity in cancer cells. Nature *483*, 570–575.

Garon, E.B. (2017). Cancer immunotherapy trials not immune from imprecise selection of patients. N. Engl. J. Med. *376*, 2483–2485.

Goodman, A.M., Kato, S., Bazhenova, L., Patel, S.P., Frampton, G.M., Miller, V., Stephens, P.J., Daniels, G.A., and Kurzrock, R. (2017). Tumor mutational burden as an independent predictor of response to immunotherapy in diverse cancers. Mol. Cancer Ther. *16*, 2598–2608.

Hornberger, G.M., and Spear, R.C. (1981). An approach to the preliminary-analysis of environmental systems. Environ. Manage. *12*, 7–18.

Jackson, S.J., and Thomas, G.J. (2017). Human tissue models in cancer research: looking beyond the mouse. Dis. Model. Mech. *10*, 939–942.

Jahnke, H.G., Poenick, S., Maschke, J., Kendler, M., Simon, J.C., and Robitzki, A.A. (2014). Direct chemosensitivity monitoring ex vivo on undissociated melanoma tumor tissue by impedance spectroscopy. Cancer Res. *74*, 6408–6418.

Jenkins, R.W., Aref, A.R., Lizotte, P.H., Ivanova, E., Stinson, S., Zhou, C.W., Bowden, M., Deng, J., Liu, H., Miao, D., et al. (2018). Ex vivo profiling of PD-1 blockade using organotypic tumor spheroids. Cancer Discov. *8*, 196–215.

Kakimi, K., Karasaki, T., Matsushita, H., and Sugie, T. (2017). Advances in personalized cancer immunotherapy. Breast Cancer *24*, 16–24.

Karekla, E., Liao, W.J., Sharp, B., Pugh, J., Reid, H., Quesne, J.L., Moore, D., Pritchard, C., MacFarlane, M., and Pringle, J.H. (2017). Ex vivo explant cultures of non-small cell lung carcinoma enable evaluation of primary tumor responses to anticancer therapy. Cancer Res. *77*, 2029–2039.

Kieper, W.C., Prlic, M., Schmidt, C.S., Mescher, M.F., and Jameson, S.C. (2001). Il-12 enhances CD8 T cell homeostatic expansion. J. Immunol. *166*, 5515–5521.

Maciejko, L., Smalley, M., and Goldman, A. (2017). Cancer immunotherapy and personalized medicine: emerging technologies and biomarker-based approaches. J. Mol. Biomark. Diagn. *8*, 350.

Majumder, B., Baraneedharan, U., Thiyagarajan, S., Radhakrishnan, P., Narasimhan, H., Dhandapani, M., Brijwani, N., Pinto, D.D., Prasath, A., Shanthappa, B.U., et al. (2015). Predicting clinical response to anticancer drugs using an ex vivo platform that captures tumour heterogeneity. Nat. Commun. *6*, 6169.

Mani, N.L., Schalper, K.A., Hatzis, C., Saglam, O., Tavassoli, F., Butler, M., Chagpar, A.B., Pusztai, L., and Rimm, D.L. (2016). Quantitative assessment of the spatial heterogeneity of tumor-infiltrating lymphocytes in breast cancer. Breast Cancer Res. *18*, 78.

Meijer, T.G., Naipal, K.A., Jager, A., and van Gent, D.C. (2017). Ex vivo tumor culture systems for functional drug testing and therapy response prediction. Future Sci. OA *3*, FSO190.

Riaz, N., Havel, J.J., Makarov, V., Desrichard, A., Urba, W.J., Sims, J.S., Hodi, F.S., Martin-Algarra, S., Mandal, R., Sharfman, W.H., et al. (2017). Tumor and microenvironment evolution during immunotherapy with nivolumab. Cell *171*, 934–949.e16.

Ruggeri, B.A., Camp, F., and Miknyoczki, S. (2014). Animal models of disease: pre-clinical animal models of cancer and their applications and utility in drug discovery. Biochem. Pharmacol. *87*, 150–161.

Samson, D.J., Seidenfeld, J., Ziegler, K., and Aronson, N. (2004). Chemotherapy sensitivity and resistance assays: a systematic review. J. Clin. Oncol. *22*, 3618–3630.

Saraiva, M., and O'Garra, A. (2010). The regulation of IL-10 production by immune cells. Nat. Rev. Immunol. *10*, 170–181.

Sharma, S.V., Haber, D.A., and Settleman, J. (2010). Cell line-based platforms to evaluate the therapeutic efficacy of candidate anticancer agents. Nat. Rev. Cancer *10*, 241–253.

Silva, A., Silva, M.C., Sudalagunta, P., Distler, A., Jacobson, T., Collins, A., Nguyen, T., Song, J., Chen, D.T., Chen, L., et al. (2017). An ex vivo platform for the prediction of clinical response in multiple myeloma. Cancer Res. *77*, 3336–3351.

Spitzer, M.H., Carmi, Y., Reticker-Flynn, N.E., Kwek, S.S., Madhireddy, D., Martins, M.M., Gherardini, P.F., Prestwood, T.R., Chabon, J., Bendall, S.C., et al. (2017). Systemic immunity is required for effective cancer immunotherapy. Cell *168*, 487–502.e5.

Tannock, I.F., and Hickman, J.A. (2016). Limits to personalized cancer medicine. N. Engl. J. Med. *375*, 1289–1294.

Wayteck, L., Breckpot, K., Demeester, J., De Smedt, S.C., and Raemdonck, K. (2014). A personalized view on cancer immunotherapy. Cancer Lett. *352*, 113–125.

Yuan, Y. (2016). Spatial heterogeneity in the tumor microenvironment. Cold Spring Harb. Perspect. Med. *6*, a026583.

Zhang, H., and Chen, J. (2018). Current status and future directions of cancer immunotherapy. J. Cancer *9*, 1773–1781.

Zi, Z. (2011). Sensitivity analysis approaches applied to systems biology models. IET Syst. Biol. *5*, 336.

Zi, Z., Cho, K.H., Sung, M.H., Xia, X., Zheng, J., and Sun, Z. (2005). In silico identification of the key components and steps in IFN-gamma induced JAK-STAT signaling pathway. FEBS Lett. *579*, 1101–1108.

iScience, Volume *23*

Supplemental Information

Integrating Systems Biology and an *Ex Vivo* Human Tumor Model Elucidates PD-1 Blockade Response Dynamics

Munisha Smalley, Michelle Przedborski, Saravanan Thiyagarajan, Moriah Pellowe, Amit Verma, Nilesh Brijwani, Debika Datta, Misti Jain, Basavaraja U. Shanthappa, Vidushi Kapoor, Kodaganur S. Gopinath, D.C. Doval, K.S. Sabitha, Gaspar Taroncher-Oldenburg, Biswanath Majumder, Pradip Majumder, Mohammad Kohandel, and Aaron Goldman

N	50	
Age in years, median (range)	54 (21-80)	
Gender		
Male	20	40%
Female	29	58%
Not Reported	1	2%
Tumor Stage		
T4N2M0	37	74%
T3N0M0	1	2%
T3N1M0	1	2%
T3N2M0	1	2%
T4N1M0	3	6%
Not Reported	7	14%
Tumor Site		
Palate	2	4%
Maxilla	2	4%
Tongue	5	10%
Lower alveolus	10	20%
Buccal Mucosa	25	50%
Others	6	12%

Figure S1: Patient demographics head and neck squamous cell carcinoma (N=50). Related to Figure 1.

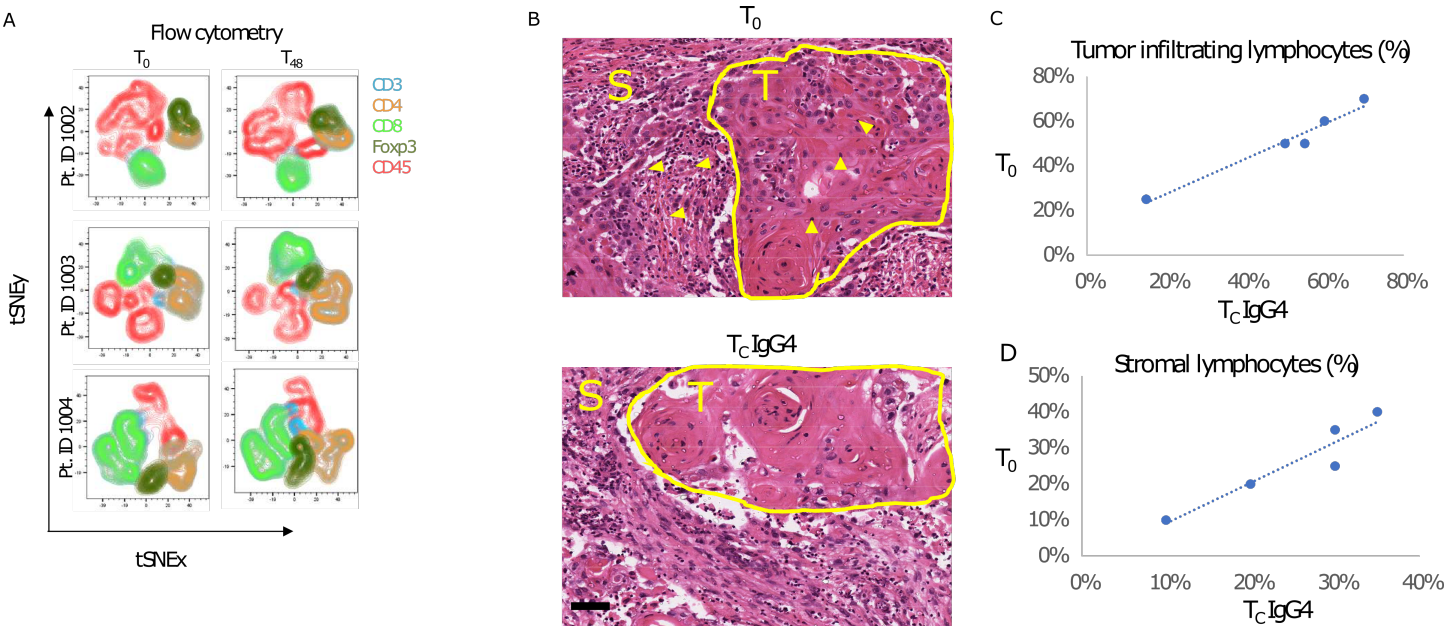

Figure S2: Profiling spatio-temporal immune fidelity comparing T_0 with unstimulated vehicle control (IgG4). Related to Figure 1. A. tSNE visualization of the tumor infiltrated immune population in baseline (T_0) and the ex-vivo vehicle control (IgG4) culture (48h) for 3 patient samples. The data is generated from flow cytometry of 3000 merged events for each sample with further sub-gating of the main T-cell populations. B. Representative H&E from HNSCC tumors at 200X magnification. Yellow line demarcates tumor (T) from stroma (S). Arrowheads indicate lymphocytes, shown as examples. Scale bar = 40mm. C-D. Blinded quantification by a clinical pathologist was performed to determine the percent (%) of tumor infiltrated lymphocytes (TIL) (B) or stromal lymphocytes (C). Linear regression and correlation of TIL and stromal lymphocytes in a pair-wise fashion of T_0 (baseline), and the patient-matched T_C Vehicle.

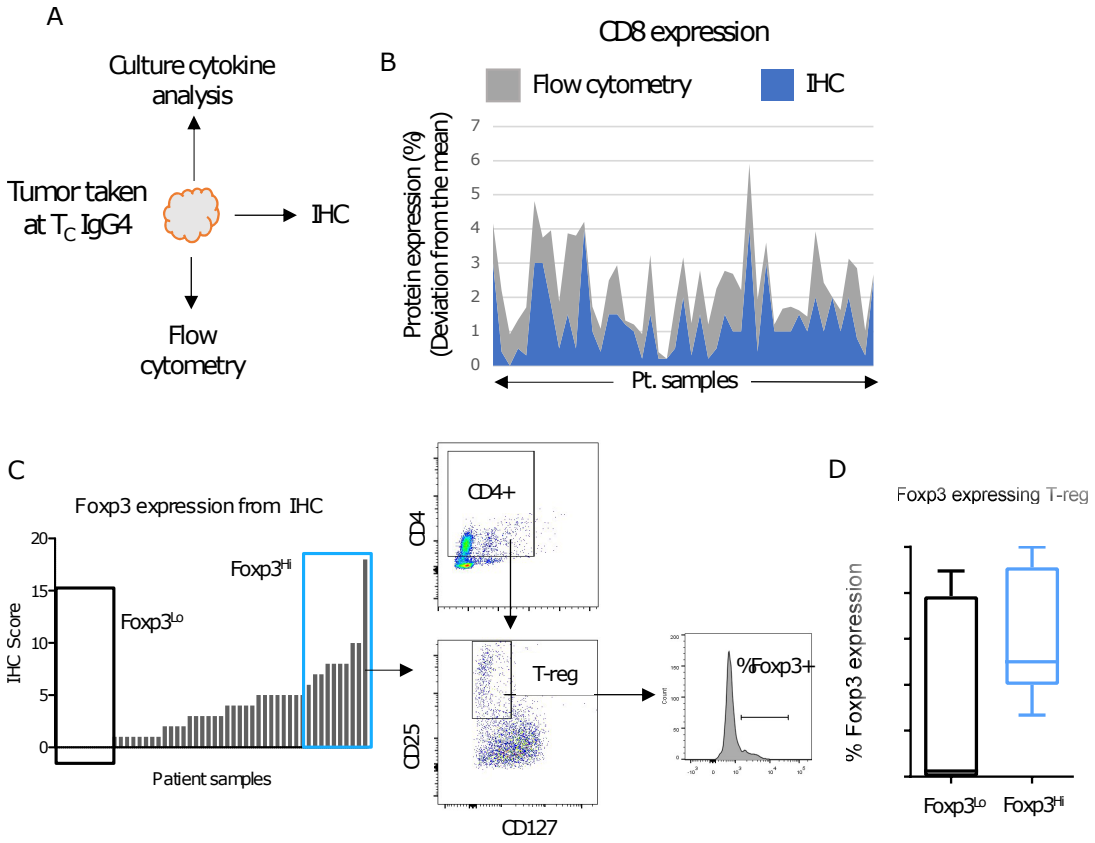

Figure S3: Testing preservation of immuno-biology by cross-analyzing multiple assays after culture, ex vivo. Related to Figure 2. A. Schematic shows the different molecular and biological assays that are employed to study tumor phenotype and culture media cytokines. B. Graph overlays the % CD8 protein expression determined by flow cytometry and immunohistochemistry (IHC). Data plotted as deviation from the mean of the respective analysis (IHC or flow), N=50 patient samples on x-axis. C. Histogram shows distribution of Foxp3 expression from the vehicle-treated cohort of 50 patient samples as determined by blinded quantification of IHC staining intensity by clinical pathology. Boxes indicate the highest and lowest Foxp3 expressing patient samples ($Foxp3^{Hi}$ and ^{Lo}). D. Histogram quantifies the % Foxp3 expression from T-reg cells determined by flow cytometry in the grouped patient samples $Foxp3^{Hi}$ and $Foxp3^{Lo}$ (Fig. Panel C).

Transparent methods

1 Systems biology model

Given the experimental measurements of cytokine expression and relative T-cell populations in ex-vivo human tumor cultures, and taking into account well-established immune cell interactions in the literature, we developed the interaction network depicted in Figure 4 of the manuscript.

An explanation of each of the cellular and protein species appearing in Figure 4 is presented in Table S1, along with its variable representation in the mathematical equations.

Table S1: Cellular and protein species in the interaction network in Figure 4.

Cellular species	**Description**	**Mathematical representation**
CD4+ Th0	Naive helper (CD4+) T-cell population	T_{N4}
CD4+ Th1	Type 1 helper T-cell population	Th_1
CD4+ Th2	Type 2 helper T-cell population	Th_2
Naive CD8+	Naive cytotoxic (CD8+) T-cell population	T_{N8}
CD8+ Tc	Cytotoxic (CD8+) T-cell population	T_c
DC	Dendritic cell population	–
Cancer	Cancer cell population	C
Protein species	**Description**	**Mathematical representation**
IL-4	Concentration of interleukin 4	$[IL\text{-}4]$
IL-6	Concentration of interleukin 6	$[IL\text{-}6]$
IL-12	Concentration of interleukin 12	$[IL\text{-}12]$
IFNγ	Concentration of interferon gamma	$[IFN\gamma]$
PD-1	Concentration of programmed cell death protein 1	$[PD\text{-}1]$
PD-L1	Concentration of programmed death-ligand 1	$[PD\text{-}L1]$
PD-1:PD-L1	Concentration of PD-1:PD-L1 protein complex	$[PD\text{-}1{:}PD\text{-}L1]$
Drug species	**Description**	**Mathematical representation**
Nivolumab	Concentration of the PD-1 inhibitor Nivolumab	$[A]$
–	Concentration of Nivolumab:PD-1 complex	$[A : PD\text{-}1]$

Below we explain each interaction in the network, along with its mathematical formulation, in addition to the key assumptions in the model. For each cellular species, it is assumed that cells proliferate via mitosis and die at rates that are proportional to their population size.

1. Time evolution of naive helper (CD4+) T-cell population:

$$\frac{dT_{N4}}{dt} = n_4 T_{N4} - \left(d_{\text{1-12}} T_{N4} \frac{[IL\text{-}12]}{q_{dIL12} + [IL\text{-}12]} + d_{\text{1-}IFN} T_{N4} \frac{[IFN\gamma]}{q_{IFN\text{-}1} + [IFN\gamma]} \right) \left(\frac{s_1}{s_1 + [PD\text{-}1 : PD\text{-}L1]} \right) - \left(d_2 T_{N4} \frac{[IL\text{-}4]}{q_{dIL4} + [IL\text{-}4]} \right) \left(\frac{s_2}{s_2 + [PD\text{-}1 : PD\text{-}L1]} \right) \quad (1)$$

The first term describes the net proliferation of T_{N4} cells. The next two terms describe the differentiation of T_{N4} cells into Th_1 cells in the presence of IL-12 (Yates et al., 2000) (term 2) and IFNγ (Diehl and Rincón, 2002) (term 3). Both of these differentiation processes are inhibited by the PD-1:PD-L1 complex (Freeman et al., 2006; Okazaki and Honjo, 2006; Sznol and Chen, 2013). The last term describes the differentiation of T_{N4} cells into Th_2 cells in the presence of IL-4 (Diehl and Rincón, 2002; Yates et al., 2000), which is inhibited by the PD-1:PD-L1 complex (Freeman et al., 2006; Okazaki and Honjo, 2006; Sznol and Chen, 2013).

2. Time evolution of type 1 helper T-cell population:

$$\frac{dTh_1}{dt} = n_1 Th_1 + \left(d_{1\text{-}12} T_{N4} \frac{[IL\text{-}12]}{q_{dIL12} + [IL\text{-}12]} + d_{1\text{-}IFN} T_{N4} \frac{[IFN\gamma]}{q_{IFN\text{-}1} + [IFN\gamma]} \right) \left(\frac{s_1}{s_1 + [PD\text{-}1 : PD\text{-}L1]} \right) \tag{2}$$

The first term describes the net proliferation of Th_1 cells. The remaining terms describe the increase in the Th_1 cell population due to the differentiation of T_{N4} cells into Th_1 cells in the presence of IL-12 (Yates et al., 2000) (term 2) and IFNγ (Diehl and Rincón, 2002) (term 3), which is inhibited by the PD-1:PD-L1 complex (Freeman et al., 2006; Okazaki and Honjo, 2006; Sznol and Chen, 2013).

3. Time evolution of type 2 helper T-cell population:

$$\begin{aligned} \frac{dTh_2}{dt} = & \left(g_2 Th_2 + g_{2\text{-}4} Th_2 \frac{[IL\text{-}4]}{q_{gIL4} + [IL\text{-}4]} \right) \left(\frac{r_{IFN}}{r_{IFN} + [IFN\gamma]} \right) \\ & + \left(d_2 T_{N4} \frac{[IL\text{-}4]}{q_{dIL4} + [IL\text{-}4]} \right) \left(\frac{s_2}{s_2 + [PD\text{-}1 : PD\text{-}L1]} \right) - \delta_2 Th_2 \end{aligned} \tag{3}$$

The first term describes the proliferation of Th_2 cells due to mitosis, which is upregulated by IL-4 (Diehl and Rincón, 2002; Yates et al., 2000) (term 2). However, this cell proliferation is inhibited by IFNγ (Fishman and Perelson, 1994). The next term describes the increase in Th_2 population resulting from the differentiation of T_{N4} cells into Th_2 cells in the presence of IL-4 (Diehl and Rincón, 2002; Yates et al., 2000) (term 3), which is inhibited by the PD-1:PD-L1 (Freeman et al., 2006; Okazaki and Honjo, 2006; Sznol and Chen, 2013) complex. The last term describes natural death of the Th_2 cells.

4. Time evolution of naive cytotoxic (CD8+) T-cell population:

$$\frac{dT_{N8}}{dt} = n_8 T_{N8} - d_c T_{N8} \left(\frac{Th_1}{q_1 + Th_1} \right) \left(\frac{s_C}{s_C + [PD\text{-}1 : PD\text{-}L1]} \right) \tag{4}$$

The first term describes the net proliferation of T_{N8} cells. The second term describes the differentiation of T_{N8} cells into T_c cells in the presence of Th_1 (Ridge et al., 1998; Sakaguchi, 2000), which is inhibited by the PD-1:PD-L1 complex (Freeman et al., 2006; Okazaki and Honjo, 2006; Sznol and Chen, 2013).

5. Time evolution of cytotoxic (CD8+) T-cell population:

$$\frac{dT_c}{dt} = n_c T_c + g_{c-12} T_c \frac{[IL-12]}{q_{gIL12} + [IL-12]} + d_c T_{N8} \left(\frac{Th_1}{q_1 + Th_1} \right) \left(\frac{s_c}{s_c + [PD\text{-}1 : PD\text{-}L1]} \right) \tag{5}$$

The first term describes the net proliferation of T_c cells, which is upregulated by IL-12 (Lasek et al., 2014) (term 2). The third term describes the increase in the T_c cell population due to the differentiation of T_{N8} cells into T_c cells in the presence of DCs that have been activated by Th_1 (Ridge et al., 1998; Sakaguchi, 2000). This differentiation process is inhibited by the PD-1:PD-L1 complex (Freeman et al., 2006; Okazaki and Honjo, 2006; Sznol and Chen, 2013).

6. Time evolution of cancer cell population:

$$\frac{dC}{dt} = n_{Can} C - k_c C T_c \tag{6}$$

The first term describes the net proliferation of cancer cells and the second term describes the killing of cancer cells by T_c cells through mechanisms such as granzyme/perforin-induced apoptosis (Freeman et al., 2006; Trapani and Smyth, 2002).

7. Time evolution of IFN-γ concentration:

$$\frac{d[IFN\gamma]}{dt} = p_{1\text{-}IFN} Th_1 \left(\frac{r_{IL4}}{r_{IL4} + [IL\text{-}4]}\right)\left(\frac{r_{IL6}}{r_{IL6} + [IL\text{-}6]}\right) + p_{c\text{-}IFN} T_c - \delta_{IFN}[IFN\gamma] \tag{7}$$

Term one describes the secretion of IFNγ by Th_1 cells (Diehl and Rincón, 2002; Fishman and Perelson, 1994; Yates et al., 2000), which is inhibited by IL-4 (Fishman and Perelson, 1999) and IL-6 (Diehl and Rincón, 2002). The second term describes the secretion of IFNγ by T_c cells (Freeman et al., 2006), and the third term describes the natural decay of IFNγ.

8. Time evolution of IL-4 concentration:

$$\frac{d[IL\text{-}4]}{dt} = p_{2\text{-}4} Th_2 + p_{2\text{-}4\text{-}6} Th_2 \left(\frac{[IL\text{-}6]}{q_{IL6} + [IL\text{-}6]}\right) - \delta_{IL4}[IL\text{-}4] \tag{8}$$

The first term describes the secretion of IL-4 by Th_2 cells (Diehl and Rincón, 2002; Fishman and Perelson, 1994; Yates et al., 2000). The second term describes the additional secretion of IL-4 by Th_2 cells in the presence of IL-6 (Diehl and Rincón, 2002; Romagnani, 1997). The third term describes the natural decay of IL-4.

9. Time evolution of IL-6 concentration:

$$\frac{d[IL\text{-}6]}{dt} = p_{2\text{-}6} Th_2 + p_{Can\text{-}6} C - \delta_{IL6}[IL\text{-}6] \tag{9}$$

Term one describes the secretion of IL-6 by Th_2 cells (Fishman and Perelson, 1994). Antigen presenting cells produce IL-6 (Diehl and Rincón, 2002; Rincón et al., 1997) and we assume that the number of antigen presenting cells is directly proportional to the number of cancer cells (term 2). The third term describes the natural decay of IL-6.

10. Time evolution of IL-12 concentration:

$$\frac{d[IL\text{-}12]}{dt} = p_{Can\text{-}12} C + p_{1\text{-}12} Th_1 - \delta_{IL12}[IL\text{-}12] \tag{10}$$

Term one describes the production of IL-12 by DCs, which we assume to be directly proportional to the number of cancer cells (Rincón et al., 1997). Term two describes the additional production of IL-12 by DCs that are activated by Th_1 cells (Macatonia et al., 1995). The third term describes the natural decay of IL-12.

11. PD-1 concentration and its time evolution:

$$[PD\text{-}1] = \rho\left(Th_1 + Th_2 + T_c\right) \tag{11}$$

$$\begin{aligned}\frac{d[PD\text{-}1]}{dt} = {} & \rho\left(\frac{dTh_1}{dt} + \frac{dTh_2}{dt} + \frac{dT_c}{dt}\right) - \beta_+[PD\text{-}1][PD\text{-}L1] + \beta_-[PD\text{-}1 : PD\text{-}L1] \\ & - \alpha_+[PD\text{-}1][A] + \alpha_-[A : PD\text{-}1]\end{aligned} \tag{12}$$

PD-1 is expressed on all activated T-cells, i.e. Th_1, Th_2, and T_c (Freeman et al., 2006; Sznol and Chen, 2013), thus the total concentration of PD-1 is proportional to the sum of the T-cell populations, as indicated in Equation (11). We make the simplifying assumption that the same amount of PD-1 is expressed on all types of T-cells, thus the proportionality constants for each population are the same.

The time evolution of PD-1 is described by Equation (12). The first three terms describe the change in the PD-1 levels due to changing T-cell populations. The fourth term describes the binding of PD-1 to PD-L1 to form the PD-1:PD-L1 complex and the fifth term describes the dissociation

of the PD-1:PD-L1 complex (Freeman et al., 2006). The last two terms describe, respectively, the binding of PD-1 to Nivolumab and the dissociation of the Nivolumab:PD-1 complex (Sznol and Chen, 2013).

12. PD-L1 concentration and its time evolution:

$$[PD\text{-}L1] = \lambda\left(Th_1 + Th_2 + T_c + C\right) + \lambda_{Can\text{-}IFN} C\left(\frac{[IFN\gamma]}{q_{IFN\text{-}PDL1} + [IFN\gamma]}\right) \tag{13}$$

$$\begin{aligned}\frac{d[PD\text{-}L1]}{dt} &= \lambda\left(\frac{dTh_1}{dt} + \frac{dTh_2}{dt} + \frac{dT_c}{dt} + \frac{dC}{dt}\right) \\ &\quad + \lambda_{Can\text{-}IFN}\frac{dC}{dt}\left(\frac{[IFN\gamma]}{q_{IFN\text{-}PDL1} + [IFN\gamma]}\right) \\ &\quad - \beta_+[PD\text{-}1][PD\text{-}L1] + \beta_-[PD\text{-}1 : PD\text{-}L1]\end{aligned} \tag{14}$$

PD-L1 is expressed on all activated T cells, i.e. Th_1, Th_2, T_c (Freeman et al., 2006; Okazaki and Honjo, 2006) as well as cancer cells (Freeman et al., 2006; Okazaki and Honjo, 2006; Sznol and Chen, 2013), thus the total concentration of PD-L1 is in part proportional to the sum of the T-cell and cancer cell populations, as indicated by the first four terms in Equation (13). We make the simplifying assumption that the PD-L1 expression is identical for all types of cells. In addition, the expression of PD-L1 by cancer cells is upregulated by IFNγ (Freeman et al., 2006; Okazaki and Honjo, 2006; Sznol and Chen, 2013), as indicated by the fifth term in Equation (13).

The time evolution of PD-L1 is described by Equation (14). The first five terms describe the change in PD-L1 levels due to changing T-cell and cancer cell populations. We make the simplifying assumption that the proteins reach their steady state values instantaneously with respect to the time scale of the changes in cell populations (i.e. the cell division rate) so that $\frac{d[IFN\gamma]}{dt} \approx 0$. The last two terms describe the binding of PD-1 to PD-L1 and the dissociation of the PD-1:PD-L1 complex (Freeman et al., 2006), respectively.

13. Time evolution of PD-1:PD-L1 complex concentration:

$$\frac{d[PD\text{-}1 : PD\text{-}L1]}{dt} = \beta_+[PD\text{-}1][PD\text{-}L1] - \beta_-[PD\text{-}1 : PD\text{-}L1] \tag{15}$$

The first term describes the binding of PD-1 to PD-L1 and the second term describes the dissociation of the PD-1:PD-L1 complex (Freeman et al., 2006).

14. Time evolution of free Nivolumab concentration:

$$\frac{d[A]}{dt} = \tilde{A}(t) - \alpha_+[A][PD\text{-}1] + \alpha_-[A : PD\text{-}1] - \delta_A[A] \tag{16}$$

The first term describes the introduction of Nivolumab into the system, which may be time-dependent, depending on the treatment schedule. The second term describes the binding of PD-1 to Nivolumab, resulting in the formation of the Nivolumab:PD-1 complex, and the third term describes the dissociation of the Nivolumab:PD-1 complex (Sznol and Chen, 2013). We make the assumption that the dissociation constant $K_\alpha \equiv \alpha_-/\alpha_+ \ll K_\beta \equiv \beta_-/\beta_+$ so that Nivolumab has a higher binding affinity for PD-1 than PD-L1 does, which allows the drug to displace PD-L1 from the PD-1:PD-L1 complex. Further, in simulations we assume that the rate of association of PD-1 is equivalent for Nivolumab and PD-L1, i.e. $\alpha_+ = \beta_+$, which removes a kinetic parameter from the system. The fourth term in the equation describes the natural decay of Nivolumab.

15. Time evolution of Nivolumab:PD-1 complex concentration:

$$\frac{d[A:PD\text{-}1]}{dt} = \alpha_{+}[A][PD\text{-}1] - \alpha_{-}[A:PD\text{-}1] \tag{17}$$

The first term describes the binding of Nivolumab with PD-1 to form the Nivolumab:PD-1 complex, and the second term describes the dissociation of the drug complex (Sznol and Chen, 2013).

In Table S2 we give a description of the kinetic parameters that appear in the above equations in the mathematical model.

Table S2: Description of the kinetic parameters in the systes biology model. Related to the interaction network in Figure 4.

Number	Name	Description
1	n_4	Net proliferation rate of T_{N4} cells
2	n_8	Net proliferation rate of T_{N8} cells
3	n_1	Net proliferation rate of Th_1 cells
4	n_c	IL12-independent net proliferation rate of T_c cells
5	n_{Can}	Net proliferation rate of cancer cells
6	g_2	IL4-independent growth rate of Th_2 cells
7	$g_{2\text{-}4}$	IL4-dependent growth rate of Th_2 cells
8	$g_{c\text{-}12}$	IL12-dependent growth rate of T_c cells
9	δ_2	Death rate of Th_2 cells
10	$d_{1\text{-}IFN}$	IFNγ-dependent differentiation rate of T_{N4} cells into Th_1 cells
11	$d_{1\text{-}12}$	IL12-dependent differentiation rate of T_{N4} cells into Th_1 cells
12	d_2	IL4-dependent differentiation rate of T_{N4} cells into Th_2 cells
13	d_c	Rate of differentiation of T_{N8} cells into T_c cells
14	k_c	Rate of cancer cell killing by T_c cells
15	$p_{1\text{-}IFN}$	Rate of production of IFNγ by Th_1 cells
16	$p_{2\text{-}4\text{-}6}$	IL6-dependent production of IL-4 by Th_2 cells
17	p_{Can-6}	Rate of production of IL-6 by antigen presenting cells (assumed proportional to the number of cancer cells)
18	p_{Can-12}	Rate of production of IL-12 by DCs (assumed proportional to the number of cancer cells)
19	δ_{IFN}	Decay rate of IFNγ
20	δ_{IL4}	Decay rate of IL-4
21	δ_{IL6}	Decay rate of IL-6
22	δ_{IL12}	Decay rate of IL-12
23	δ_A	Decay rate of Nivolumab
24	q_1	Half-maximal Th_1 cell population for T_{N8} differentiation into T_c cells

25	$q_{IFN\text{-}1}$	Half-maximal IFNγ concentration for IFNγ-dependent differentiation of T_{N4} cells into Th_1 cells
26	$q_{IFN\text{-}PDL1}$	Half-maximal IFNγ concentration for IFNγ-dependent PD-L1 expression by cancer cells
27	q_{gIL4}	Half-maximal IL-4 concentration for IL4-dependent proliferation of Th_2 cells
28	q_{dIL4}	Half-maximal IL-4 concentration for IL4-dependent differentiation of T_{N4} cells into Th_2 cells
29	q_{IL6}	Half-maximal IL-6 concentration for IL6-dependent production of IL-4 by Th_2 cells
30	q_{dIL12}	Half-maximal IL-12 concentration for IL12-dependent differentiation of T_{N4} cells into Th_1 cells
31	q_{gIL12}	Half-maximal IL-12 concentration for IL12-dependent proliferation of T_c cells
32	r_{IFN}	Half-maximal IFNγ concentration for IFNγ-dependent inhibition of Th_2 proliferation
33	r_{IL4}	Half-maximal IL-4 concentration for IL4-dependent inhibition of IFNγ production by Th_1 cells
34	r_{IL6}	Half-maximal IL-6 concentration for IL6-dependent inhibition of IFNγ production by Th_1 cells
35	ρ	Per-cell expression level of PD-1
36	λ	Per-cell expression level of PD-L1
37	$\lambda_{Can\text{-}IFN}$	IFNγ-dependent PD-L1 expression per cancer cell
38	β_+	Rate of association of PD-1 and PD-L1
39	β_-	Rate of dissociation of PD-1:PD-L1 complex
40	α_-	Rate of dissociation of Nivolumab:PD-1 complex
41	s_1	Half-maximal PD-1:PD-L1 concentration for inhibition of T_{N4} differentiation into Th_1 cells
42	s_2	Half-maximal PD-1:PD-L1 concentration for inhibition of T_{N4} differentiation into Th_2 cells
43	s_c	Half-maximal PD-1:PD-L1 concentration for inhibition of T_{N8} differentiation into T_c cells
44	$p_{1\text{-}12}$	Rate of IL-12 production by Th_1 cells
45	$p_{2\text{-}4}$	Rate of IL6-independent production of IL-4 by Th_2 cells
46	$p_{2\text{-}6}$	Rate of IL-6 production by Th_2 cells
47	$p_{c\text{-}IFN}$	Rate of IFNγ production by T_c cells

2 Systems biology parameter values

In Table S3, we present the numerical values of the parameters and initial conditions (protein levels and relative T-cell populations) that match to the average patient data (see "nominal value" column), as well as the corresponding units (see "units" column). We use the abbreviation "min" to denote a timescale of minutes. We also present a range for each parameter which was used for searching the parameter space with Matlab's genetic algorithm to match the average patient data as well as for performing the

global sensitivity analysis (see "range" column). The ranges presented for the protein levels and T-cell fractions that were obtained from the patient data are set by the minimum and maximum experimentally measured values for all patients, and were used for the global sensitivity analysis. When using the genetic algorithm to match the average patient data, the T-cell fractions were set to the average of all patients without treatment, and the protein levels were sampled from a range set by the average +/- one standard deviation, as explained in the main text.

We note that parameters 44-47 do not have a specified range since they were calculated at the beginning of each simulation by assuming the initial protein levels are steady state protein levels (Equations 7-10) using the initial T-cell population values, and additionally imposing the constraint that all parameters are non-negative. Thus with the local and global sensitivity analysis, it was necessary to re-calculate parameters 44-47 for each simulation.

To ensure that Nivolumab has a higher binding affinity for PD-1 than PD-L1 does, we also imposed the constraint (parameter 40 $<$ 0.1 parameter 39) for each simulation.

Additionally, we note that the PD-1 and PD-L1 concentrations were initialized for each simulation using Equations 11 and 13, respectively, with the initial cell populations and relevant protein level. Finally we point out that in an initial analysis, we used a larger upper bound for the net proliferation rate of cancer cells, parameter 5. In some cases, this led to nonphysical growth of the cancer population over the three day treatment window when there was no treatment response. In these cases, the model output was most sensitive to parameters controlling the CD8+ cytotoxic T-cell population and its efficiency at killing the cancer cells. We present additional important notes below the table.

Table S3: Values and ranges of the kinetic parameters, initial protein levels, and initial T-cell populations used for local and global sensitivity analysis. Related to Figures 5 and 6.

Parameter	Nominal value	Range	Units	Reference
1	2.5×10^{-1}	$\ln(2)/20 - \ln(2)$	day^{-1}	estimated from (Fishman and Perelson, 1994) (Fishman and Perelson, 1999)
2	3.5×10^{-2}	$\ln(2)/20 - \ln(2)$	day^{-1}	estimated from (Fishman and Perelson, 1994) (Fishman and Perelson, 1999)
3	4.8×10^{-2}	$\ln(2)/20 - \ln(2)$	day^{-1}	estimated from (Fishman and Perelson, 1994) (Fishman and Perelson, 1999)
4	4.1×10^{-2}	$\ln(2)/20 - \ln(2)$	day^{-1}	estimated from (Fishman and Perelson, 1994) (Fishman and Perelson, 1999)
5	7.0×10^{-3}	$\ln(2)/100 - \ln(2)/10$	day^{-1}	estimated
6	3.8×10^{-2}	$\ln(2)/20 - \ln(2)$	day^{-1}	estimated from (Fishman and Perelson, 1994) (Fishman and Perelson, 1999)
7	3.5×10^{-2}	$\ln(2)/20 - \ln(2)$	day^{-1}	estimated from (Fishman and Perelson, 1994) (Fishman and Perelson, 1999)
8	3.6×10^{-2}	$\ln(2)/20 - \ln(2)$	day^{-1}	estimated from (Fishman and Perelson, 1994) (Fishman and Perelson, 1999)

9	1.2×10^{-2}	$\ln(2)/60 - \ln(2)/7$	day^{-1}	estimated from (Fishman and Perelson, 1994) (Fishman and Perelson, 1999)
10	1.9×10^{-1}	$\ln(2)/20 - \ln(2)$	day^{-1}	estimated from (Morel et al., 1992)
11	3.6×10^{-2}	$\ln(2)/20 - \ln(2)$	day^{-1}	estimated from (Morel et al., 1992)
12	2.1×10^{-2}	$\ln(2)/20 - \ln(2)$	day^{-1}	estimated from (Morel et al., 1992)
13	2.3×10^{-2}	$\ln(2)/20 - \ln(2)$	day^{-1}	estimated from (Morel et al., 1992)
14	1.1×10^{-5}	$10^{-5} - 10^{-1}$	T_c cell$^{-1}\cdot$ day^{-1}	estimated
15	1.3×10^{-3}	$6.5 \times 10^{-4} - 1.7 \times 10^{-2}$	$\frac{\text{pg/mL}}{Th_1 \text{ cell} \cdot \text{day}}$	estimated
16	1.6×10^{-4}	$1.4 \times 10^{-7} - 1.4\times^{-2}$	$\frac{\text{pg/mL}}{Th_2 \text{ cell} \cdot \text{day}}$	estimated
17	1.8×10^{-2}	$7.2 \times 10^{-3} - 7.2 \times 10^{-1}$	$\frac{\text{pg/mL}}{\text{cancer cell} \cdot \text{day}}$	estimated
18	1.2×10^{-3}	$1.2 \times 10^{-3} - 1.4 \times 10^{-2}$	$\frac{\text{pg/mL}}{\text{cancer cell} \cdot \text{day}}$	estimated from (Lai and Friedman, 2017)
19	$\ln(2)/1000$	$\ln(2)/1000 - \ln(2)/60$	min^{-1}	estimated from (Fishman and Perelson, 1999)
20	7.0×10^{-4}	$\ln(2)/1000 - \ln(2)/60$	min^{-1}	estimated from (Fishman and Perelson, 1999)
21	$\ln(2)/1000$	$\ln(2)/1000 - \ln(2)/60$	min^{-1}	estimated from (Fishman and Perelson, 1999)
22	4.8×10^{-4}	$\ln(2)/1440 - \ln(2)/600$	min^{-1}	estimated from (Lai and Friedman, 2017)
23	4.8×10^{-2}	$\ln(2)/15 - \ln(2)/10$	day^{-1}	estimated from (Lai and Friedman, 2017)
24	1.6×10^{2}	$1 - 10^{5}$	Th_1 cells	estimated
25	4.0×10^{-1}	$10^{-3} - 10^{2}$	$[IFN\gamma]$ (pg/mL)	estimated
26	6.3×10^{-1}	$10^{-3} - 10^{2}$	$[IFN\gamma]$ (pg/mL)	estimated
27	4.03	$10^{-3} - 10^{3}$	$[IL\text{-}4]$ (pg/mL)	estimated
28	8.4×10^{-1}	$10^{-3} - 10^{3}$	$[IL\text{-}4]$ (pg/mL)	estimated
29	1.3×10^{2}	$10^{2} - 10^{4}$	$[IL\text{-}6]$ (pg/mL)	estimated
30	6.3×10^{-3}	$10^{-3} - 10^{2}$	$[IL\text{-}12]$ (pg/mL)	estimated
31	3.4×10^{-2}	$10^{-3} - 10^{2}$	$[IL\text{-}12]$ (pg/mL)	estimated
32	8.9×10^{-2}	$10^{-3} - 10^{2}$	$[IFN\gamma]$ (pg/mL)	estimated
33	7.5×10^{-1}	$10^{-1} - 10^{3}$	$[IL\text{-}4]$ (pg/mL)	estimated
34	1.4×10^{2}	$10^{2} - 10^{4}$	$[IL\text{-}6]$ (pg/mL)	estimated
35	9.9	$10^{-6} - 10^{1}$	(pg/mL)/T-cell	estimated from (Lai and Friedman, 2017)

36	1.0×10^{1}	$10^{-6} - 10^{1}$	$(\text{pg/mL})/\text{cell}$	estimated from (Lai and Friedman, 2017)
37	1.8×10^{-4}	$10^{-10} - 10^{-1}$	$(\text{pg/mL})/\text{cancer cell}$	estimated from (Lai and Friedman, 2017)
38	1.7×10^{-3}	$1.4 \times 10^{-4} - 1.4 \times 10^{-1}$	$\big((\text{pg/mL}) \cdot \text{day}\big)^{-1}$	estimated
39	1.5	$1.4 - 1.4 \times 10^{2}$	day^{-1}	estimated
40	3.5×10^{-3}	$1.4 \times 10^{-3} - 1.4 \times 10^{-1}$	$\big((\text{pg/mL}) \cdot \text{day}\big)^{-1}$	estimated
41	4.9×10^{1}	$10^{-3} - 10^{5}$	$[PD\text{-}1 : PD\text{-}L1]$ (pg/mL)	estimated
42	2.1	$10^{-3} - 10^{5}$	$[PD\text{-}1 : PD\text{-}L1]$ (pg/mL)	estimated
43	1.9×10^{1}	$10^{-3} - 10^{5}$	$[PD\text{-}1 : PD\text{-}L1]$ (pg/mL)	estimated
44	7.7×10^{-5}	see text	$\frac{\text{pg/mL}}{Th_2 \text{ cell} \cdot \text{day}}$	–
45	3.7×10^{-6}	see text	$\frac{\text{pg/mL}}{Th_2 \text{ cell} \cdot \text{day}}$	–
46	1.1×10^{-1}	see text	$\frac{\text{pg/mL}}{T_c \text{ cell} \cdot \text{day}}$	–
47	3.0×10^{-8}	see text	$\frac{\text{pg/mL}}{T_c \text{ cell} \cdot \text{day}}$	–
Protein	**Nominal value**	**Range**	**Units**	**Reference**
IFNγ	0.45	$0.18 - 482.31$	pg/mL	patient data
IL-12	1.54	$1.82 - 11.44$	pg/mL	patient data
IL-6	3339.16	$149.15 - 35884.0$	pg/mL	patient data
IL-4	0.11	$0.10 - 61.37$	pg/mL	patient data
Cell fraction	**Nominal value**	**Range**	**Units**	**Reference**
Cancer fraction	0.81	$0.1 - 0.9$*	–	estimated
TN8 fraction	0.65	$0.21 - 0.97$	–	patient data
Tc fraction	0.10	$0.0 - 0.59$	–	patient data
CD4+ fraction	0.25	$0.01 - 0.69$**	–	patient data
Th1 fraction	3.9×10^{-4}	$0 - 0.99$	–	estimated
Th2 fraction	8.6×10^{-4}	$0 - 0.99$***	–	estimated

*The tumor is assumed to consist of a population of cancer cells and a population of immune cells. Thus with the nominal values given in Table 3, 81% of the tumor is cancer cells and the remaining 19% is the total immune cell population.

**The total immune cell population consists of naive CD8+ T-cells (T_{N8}), CD8+ cytotoxic T-cells (T_c), and a population of CD4+ cells, thus we always impose the constraint (TN8 fraction + Tc fraction + CD4+ fraction) = 1.

***The CD4+ fraction is further subdivided into naive helper CD4+ T-cells (T_{N4}), type 1 helper T-cells (Th_1) and type 2 helper T-cells (Th_2), thus we always impose the constraint (Th1 fraction + Th2 fraction + TN4 fraction) = 1.

3 Ex vivo Culture

HNSCC patients were recruited from multiple hospitals in India with approval from institutional review board (IRB) and institutional ethical committee (IEC). Patient-consented tumor biopsies or surgical tissues, in addition to blood specimens were transported to Mitra Biotech, Bangalore in a transport container (Crēdo CubeTM (Peli Bio Thermal, Plymouth MN) in transport buffer containing a defined tissue culture media recipe (described in detail below) and processed within 24-48 h post-excision. The time of excision was captured on surgical reports. Both blood and tissue samples were shipped in temperature-controlled containers, also containing temperature-loggers to maintain a temperature of 4-7°C. Details of patient demography collected are outlined in Supplemental Figure 1. Quality control (QC) of the sample include: (1) absence of blood hemolysis, (2) arrival of patient tumors and blood specimens at a temperature range of 4-7°C (3) a minimum tumor content, which is evaluated by a clinical pathologist on HE-stained FFPE tissue (T0 tissue), of 20%. Approximately 50% of samples that arrived at the lab were deemed suitable, by the quality control criteria described above, to be further processed in the ex vivo system. Tumor tissues were then moved from the transport chamber into warmed (37°C) tissue culture media (recipe described in detail below), dissected into uniform slices using manual fragmentation procedures. Tissue slices were maintained in customized tumor matrix protein (TMP) coated plates as described earlier (Brijwani et al., 2017; Majumder et al., 2015). Briefly, TMP were previously identified using a tandem liquid chromatography mass spectrometry (LC/MS) approach which elucidated the varying concentrations of each protein that are typically found within head and neck tumors derived from human patients. Sterile recombinant human TMP are then coated onto tissue culture plates and used for the tissue culture procedure, outlined in Figure 1A. Tissue fragments (approximately 300 μm - 2 mm in size) were then placed into each well of a 48-well plate coated in TMP and incubated with 500 μl of tissue culture media (RPMI containing 20% fetal bovine serum, 2% autologous patient serum, penicillin, streptomycin. 1 Insulin-Transferrin-Selenium (ITS, Life Technologies. 41400-045), 1 GlutaMAX (Life Technologies. 35050-061) and 1 penicillin, streptomycin and amphotericin B (Life Technologies. 15140-122). Drug (described below) was then incubated with each tissue fragment. Experiments were performed in replicate of a maximum of four individual tissue fragments receiving drug and a minimum of three for up to 72 hours. Tissue culture media and drug removed and replaced every 24 hours. Tissue culture supernatants were collected at 0 hours (baseline) & 48-72 hours post-culture in the presence of protease and phosphatase inhibitors and stored at -80°C until further analysis. Similarly, tumor slices were collected at 0 hour (baseline) & post-culture, placed in RNAlater (Ambion, Thermo-Fisher Scientific) and processed for subsequent analyses (described in detail in each section below).

4 Drugs

The anti-PD-1 antibody, nivolumab (Opdivo, Bristol Myers Squibb) was dissolved into a 1x phosphate buffered saline (PBS) at pH7.2 and stored in aliquots at -80°C for one-time use (i.e. not repeated freeze/thawed). Isotype control antibody (Ultra-LEAF^{TM} Purified Human IgG4 Isotype Control, Biolegend catalog # 403702) was used to compare as a vehicle control or negative control against the test antibody, i.e. nivolumab. IgG4 control and nivolumab were used at the concentration of 132 μg/ml. This dose was selected based on the published clinical cmax area under the curve (Brahmer et al., 2010).

5 Multiplex Cytokine Analysis

The tissue culture supernatants (25 μl) were used to measure the secreted profile of cytokine analytes, incubated with 25 μl of beads for 1 h and 25 μl biotinylated detection antibody for 30 min. The complex

was spiked with 25 μl of Streptavidin-PE and analyzed for cytokine profiling using Luminex200 (Luminex, USA) platform. The cell-free supernatant (25 μl) was run on one or multiple Millipore Milliplex plates, customized for the analytes selected. For each plate, a set of standard curves was run to ensure accurate evaluation of the concentration of each analyte and the integrity of the assay. Each plate was read on the Luminex 200. Concentrations of each analyte was interpolated from their respective standard curve using the Milliplex Analyst software (Millipore, USA). Data from multiple plates were compiled and analyte fold changes, relative to vehicle controls, was calculated using an appropriate graphing and statistical software.

6 Enzymatic Dissociation of Tumor Tissues

For flow cytometric analysis, tumor tissues post-culture ex vivo in the presence of vehicle (IgG4) or nivolumab were subject to single cell dissociation. Tissue slices were transferred into gentle MACS C tube in FBS free media containing enzyme mix (Enzyme H, Enzyme R, and Enzyme A) (Tumor Dissociation Kit, Miltenyi Biotec, USA). Tissue slices were dissociated using the h_tumor_01.01, h_tumor_02.01 and h_tumor_03.01 dissociation programs in gentle MACS Dissociator (Miltenyi Biotec). The enzyme mix was inactivated after incubation at 37°C for 30 min. The single cell suspension was passed through 70 μm strainer, washed and resuspended in FACS buffer (2% FBS in PBS) for subsequent staining.

7 Flow Cytometry

Following enzymatic dissociation, single cell suspensions from T0 baseline and T72 culture (72 hours post culture vehicle control) obtained from culture were stained with the following antibodies: anti-CD45 AF700 (clone 560566), anti-CD4 Pe-Cy7 (557852), anti CD8-APC-H7(641400), anti-CD14 PE-Cy5.5 (562692), anti-Foxp3 PE (560082), all from BD Bioscience, anti-CD3 BV510 (317332, Biolegend). The live cells were gated using Live-Dead Blue fixable cell stain method (L23105, Thermo Fisher Scientific). Flow cytometry acquisition was performed in BD LSR Fortessa. To assess the phenotypic modulation post treatment with the test arms, single cell suspensions obtained following enzymatic dissociation were divided in two parts: one part was stained with a CD8 panel and the other with a T-reg panel. The following antibodies were used for flow cytometry analysis: CD8 cocktail (anti- IFNγ FITC/ anti-CD69 PE/ anti-CD8 PerCP-Cy^{TM}5.5/ anti-CD3 APC, 346048, BD Bioscience), T-reg Cocktail (anti-CD4 FITC/ anti-CD25 PE-Cy7/ anti-CD127 Alexa Fluor 647,560249, BD Bioscience) and anti-Foxp3 PE (560082, BD Bioscience). All antibodies were used according to manufacturers instructions along with recommended buffers. Flow cytometry acquisition was performed in BD FACS Canto II (BD Bioscience). All data were analysed using FlowJo software. For tSNE plots for T0 baseline vs T72 comparison, cells were first gated on live and singlets, then down-sampled and concatenated prior to visualization with the built in tSNE module in FlowJo. The settings for computation were as follows: iterations = 1000; perplexity = 20, learning rate = 200, theta = 0.5.

8 Immunohistochemistry

Tissue sections were deparaffinized followed by rehydration and soaked in Antigen Unmasking Solution (Vector Labs) for 10 minutes followed by retrieval. Following protein blocking, FFPE tissue sections were incubated with appropriate primary antibodies (anti-Ki-67, Dako, envision kit, 1:400, and anti-caspase 3c (rabbit) from CST, 1:600 dilution). Validated positive and negative controls were included for every IHC assay. Each IHC result was evaluated by two independent experts and any differences in observation both experts came to a consensus as described previously (Bressenot et al.,

2009; Vaira et al., 2010). Antibodies used: anti-human CD8 antibody (rabbit polyclonal, Abcam, cat Ab4055,1:300 dilution), anti-human-PD-L1 antibody (rabbit monoclonal, Cell Signaling Technology, cat# 13684, clone E1L3N, 1:100 dilution) and anti-human FoxP3 antibody (mouse monoclonal, Abcam, UK, cat# ab22510, 1:100 dilution). A compatible secondary antibody (100 μl) was incubated for an optimized time period in humidified condition (Signal stain(R) Boost IHC detection reagent HRP Rabbit, Cell Signaling Technology- 8114s or Signal stain(R) Boost IHC detection reagent HRP Mouse Cell Signaling Technology- 8125s wherever applicable). Staining was visualized with freshly prepared DAB + Chromogen followed by DAB detection system (Vector Lab). Slides were counterstained in Harris hematoxylin (Merck-6092530121730), dehydrated through graded ethanol solutions, cleared in xylene and cover slipped. IHC slides were examined using a light microscope (DM2500, Leica, USA) and quantified by scoring the level of positivity and intensity on a scale of 0-100 by a clinical pathologist. All slides were examined independently by two experienced histopathologists in a blinded fashion. Representative images were captured in 200X magnification using Leicas inbuilt camera (DFC 450 C).

9 Bioinformatics

Published data used for analysis from either NanoString (Chen et al. (Chen et al., 2016)) or RNA Seq (Riaz et al. (Riaz et al., 2017)) were obtained from the published supplemental data or GEO accession: GSE91061, respectively. The Riaz et al data set was filtered for samples that did not have the exact pre/on treatment pair and for nave-immune checkpoint inhibitor treated patient samples, resulting in a total of 17 samples used for analysis in this study. The genes used to identify a Th1-related phenotype were compiled from various literature sources and include: CASP1, CCL3, CCL4, CCRI1, CCR2, CCR5, CD38, CLU, CD55, CSF2, CTLA4, CXCR3, GATA3, IFNG, NKFBIA, IL12RB2, LTA, PRF1, CCL5, SPP1, STAT1, STAT4, TBX21, TNF. The variance calculation for control and treatment groups was performed to detect the change in variance of a gene signature between samples after drug pressure. Data was transformed to log2 Z-scores to obtain mean of 0 and standard deviation of 1. To calculate the same in Cytokines, Flow Cytometry and IHC datasets a small value of 0.1 was added to the data before log2 transformation to prevent infinite values after log, keeping the rest of the analysis the same.

10 Statistical Analysis

1-sample Kolmogorov-Smirnov test was used to assess the data distribution normality. A non-parametric Mann-Whitney U test was used to determine statistical significance with a two-tailed p-value. Spearman rho was calculated to determine the correlation coefficient between paired samples in the data sets from Figure 1C. GraphPad Prism v 7.0 was used to perform statistical calculations.

11 Mathematical modeling and numerical simulations

The interactions between different immune cell populations, between immune cells and cytokines, and between immune cells and cancer cells that were included in the systems biology model are well established in the literature (see Section 1 for more details).

We briefly describe here the cell populations comprising the model and the main interactions. The model consists of a population of nave CD4+ helper T-cells (CD4+ Th0), type1 helper T-cells (CD4+ Th1), type 2 helper T-cells (CD4+ Th2), nave CD8+ cytotoxic T-cells (nave CD8+), CD8+ cytotoxic T-cells (CD8+ Tc), and a cancer cell population. Cell proliferation and natural death are assumed for all cell populations in the model. Additionally, the CD4+ Th0 cells can differentiate into either CD4+ Th1

cells or CD4+ Th2 cells. The first differentiation process is mediated by the cytokines IL-4 and IL-6. IL-12 and IFNγ mediate the second differentiation process. Nave CD8+ cells differentiate into CD8+ Tc cells in the presence of CD4+ Th1 cells, and the proliferation rate of CD8+ Tc cells is increased by IL-12 expression level. CD8+ Tc cells kill the cancer cells. All activated T-cells (CD4+ Th1, CD4+ Th2, CD8+ Tc) express PD-1 and PD-L1. Cancer cells also express PD-L1, which is mediated by IFNγ expression. PD-1 and PD-L1 form a protein complex which inhibits all T-cell differentiation processes. The production of cytokines depends on the T-cell populations and cancer cell population, and there are several feedback loops which affect the production rates. We refer the reader to Section 1 for specific details.

To determine the values of the nominal parameters, we used the MATLAB genetic algorithm with the ode15s solver to integrate the system of coupled ODEs, while simulating the treatment protocol and forcing the simulated cytokine and T-cell populations to match to the average patient data. While performing the parameter search using MATLAB genetic algorithm, the parameter ranges were set to previously reported biologically relevant ranges when possible (see Section 1 for more details). To simulate the 72-hour treatment protocol on the model system we administered 132 μg/ml of nivolumab at t=0 h, t=24 h, and t=48 h. Drug washout between subsequent doses of nivolumab was simulated by setting the free drug level to zero immediately before administering the next dose. Over the treatment window, the cytokine expression levels were forced to lie between average +/- one standard deviation of the patient data (with nivolumab treatment) at t=24 h, 48 h, and 72 h, and the T-cell populations were forced to lie between average +/- one standard deviation at t=72 h (with nivolumab treatment). Using this approach, it is conceivable that there could be many sets of parameters that fit the average patient data. The nominal parameter set that we obtained is presented in Table 3 below.

To perform the local sensitivity analysis, each kinetic parameter was varied one-at-a-time by +1%, and the system was subsequently simulated with the perturbed parameter value. The relative sensitivity, S, was then calculated using the following equation,

$$S = \frac{(\tilde{C}_{72} - C_{72})/C_{72}}{(\tilde{p} - p)/p},$$

where p is the nominal parameter value, $\tilde{p}$ is the perturbed parameter value, C_{72} is the size of the cancer cell population after the 72-hour treatment protocol with the nominal parameter set, and $\tilde{C}_{72}$ is the size of the cancer cell population after the 72-hour treatment protocol with the perturbed parameter set. This process was repeated for all parameters in the model, as well as for the initial cytokine levels and initial T-cell populations.

To efficiently sample the parameter space (i.e. to generate the parameter sets and initial conditions) for the global sensitivity analysis, the Latin hypercube sampling method (McKay et al., 1979) was used. The ranges of the kinetic parameters, initial cytokine levels, and initial T-cell levels used for the Latin hypercube sampling are presented in Table 3 below; the ranges for initial cytokine levels and initial T-cell levels were set by the lowest and highest values expressed in the untreated patient data. In order to elucidate which patient features were necessary to capture the variability in patient response to treatment, the global sensitivity analysis was conducted in several steps. First, the kinetic parameters in the model were held fixed to the nominal values used for the local sensitivity analysis and the initial T-cell populations were fixed to the average values of the patient data (without treatment). Several thousand treatment simulations were then performed, where the initial cytokine levels were sampled within the range presented in Table 3 below. Next, we kept the kinetic parameters held fixed and varied all the initial cytokine levels and initial T-cell populations simultaneously. Specifically, using the Latin hypercube sampling method, 50,000 sets of initial cytokine levels and T-cell levels were generated within the ranges presented in Table 3, then the 72-hour treatment protocol was simulated for each set of initial conditions. Lastly, we allowed all the kinetic parameters and initial conditions to vary. Particularly, we generated 50,000 sets of parameters/initial conditions, which resulted in a large variability in the nature and the strength of the response to treatment.

References

J. R. Brahmer, C. G. Drake, I. Wollner, J. D. Powderly, J. Picus, W. H. Sharfman, E. Stankevich, A. Pons, T. M. Salay, T. L. McMiller, et al. Phase i study of single-agent anti–programmed death-1 (mdx-1106) in refractory solid tumors: safety, clinical activity, pharmacodynamics, and immunologic correlates. *Journal of clinical oncology*, 28(19):3167, 2010.

A. Bressenot, S. Marchal, L. Bezdetnaya, J. Garrier, F. Guillemin, and F. Plénat. Assessment of apoptosis by immunohistochemistry to active caspase-3, active caspase-7, or cleaved parp in monolayer cells and spheroid and subcutaneous xenografts of human carcinoma. *Journal of Histochemistry & Cytochemistry*, 57(4):289–300, 2009.

N. Brijwani, M. Jain, M. Dhandapani, F. Zahed, P. Mukhopadhyay, M. Biswas, D. Khatri, V. D. Radhakrishna, B. Majumder, P. Radhakrishnan, et al. Rationally co-targeting divergent pathways in kras wild-type colorectal cancers by canscript technology reveals tumor dependence on notch and erbb2. *Scientific reports*, 7(1):1–12, 2017.

P.-L. Chen, W. Roh, A. Reuben, Z. A. Cooper, C. N. Spencer, P. A. Prieto, J. P. Miller, R. L. Bassett, V. Gopalakrishnan, K. Wani, et al. Analysis of immune signatures in longitudinal tumor samples yields insight into biomarkers of response and mechanisms of resistance to immune checkpoint blockade. *Cancer discovery*, 6(8):827–837, 2016.

S. Diehl and M. Rincón. The two faces of il-6 on th1/th2 differentiation. *Molecular immunology*, 39(9): 531–536, 2002.

M. A. Fishman and A. S. Perelson. Th1/th2 cross regulation. *Journal of theoretical biology*, 170(1): 25–56, 1994.

M. A. Fishman and A. S. Perelson. Th1/th2 differentiation and cross-regulation. *Bulletin of mathematical biology*, 61(3):403–436, 1999.

G. J. Freeman, E. J. Wherry, R. Ahmed, and A. H. Sharpe. Reinvigorating exhausted hiv-specific t cells via pd-1–pd-1 ligand blockade. *Journal of Experimental Medicine*, 203(10):2223–2227, 2006.

X. Lai and A. Friedman. Combination therapy of cancer with cancer vaccine and immune checkpoint inhibitors: A mathematical model. *PLoS One*, 12(5):e0178479, 2017.

W. Lasek, R. Zagożdżon, and M. Jakobisiak. Interleukin 12: still a promising candidate for tumor immunotherapy? *Cancer Immunology, Immunotherapy*, 63(5):419–435, 2014.

S. E. Macatonia, N. A. Hosken, M. Litton, P. Vieira, C.-S. Hsieh, J. A. Culpepper, M. Wysocka, G. Trinchieri, K. M. Murphy, and A. O'Garra. Dendritic cells produce il-12 and direct the development of th1 cells from naive cd4+ t cells. *The Journal of Immunology*, 154(10):5071–5079, 1995.

B. Majumder, U. Baraneedharan, S. Thiyagarajan, P. Radhakrishnan, H. Narasimhan, M. Dhandapani, N. Brijwani, D. D. Pinto, A. Prasath, B. U. Shanthappa, et al. Predicting clinical response to anticancer drugs using an ex vivo platform that captures tumour heterogeneity. *Nature communications*, 6(1): 1–14, 2015.

M. D. McKay, R. J. Beckman, and W. J. Conover. Comparison of three methods for selecting values of input variables in the analysis of output from a computer code. *Technometrics*, 21(2):239–245, 1979.

B. F. Morel, J. Kalagnanam, and P. A. Morel. Mathematical modeling of th1-th2 dynamics. In *Theoretical and experimental insights into immunology*, pages 171–190. Springer, 1992.

T. Okazaki and T. Honjo. The pd-1–pd-l pathway in immunological tolerance. *Trends in immunology*, 27 (4):195–201, 2006.

N. Riaz, J. J. Havel, V. Makarov, A. Desrichard, W. J. Urba, J. S. Sims, F. S. Hodi, S. Martín-Algarra, R. Mandal, W. H. Sharfman, et al. Tumor and microenvironment evolution during immunotherapy with nivolumab. *Cell*, 171(4):934–949, 2017.

J. P. Ridge, F. Di Rosa, and P. Matzinger. A conditioned dendritic cell can be a temporal bridge between a cd4+ t-helper and a t-killer cell. *Nature*, 393(6684):474, 1998.

M. Rincón, J. Anguita, T. Nakamura, E. Fikrig, and R. A. Flavell. Interleukin (il)-6 directs the differentiation of il-4–producing cd4+ t cells. *Journal of Experimental Medicine*, 185(3):461–470, 1997.

S. Romagnani. The th1/th2 paradigm. *Immunology today*, 18(6):263–266, 1997.

S. Sakaguchi. Regulatory t cells: key controllers of immunologic self-tolerance. *Cell*, 101(5):455–458, 2000.

M. Sznol and L. Chen. Antagonist antibodies to pd-1 and b7-h1 (pd-l1) in the treatment of advanced human cancerresponse. *Clinical Cancer Research*, 19(19):5542–5542, 2013.

J. A. Trapani and M. J. Smyth. Functional significance of the perforin/granzyme cell death pathway. *Nature Reviews Immunology*, 2(10):735, 2002.

V. Vaira, G. Fedele, S. Pyne, E. Fasoli, G. Zadra, D. Bailey, E. Snyder, A. Faversani, G. Coggi, R. Flavin, et al. Preclinical model of organotypic culture for pharmacodynamic profiling of human tumors. *Proceedings of the National Academy of Sciences*, 107(18):8352–8356, 2010.

A. Yates, C. Bergmann, J. L. Van Hemmen, J. Stark, and R. Callard. Cytokine-modulated regulation of helper t cell populations. *Journal of theoretical biology*, 206(4):539–560, 2000.